# Pressure forces on sediment particles in turbulent open-channel flow: a laboratory study

## Mohammad Amir[1,†], Vladimir I. Nikora[1] and Mark T. Stewart[1]

[1]School of Engineering, University of Aberdeen, Aberdeen AB24 3UE, UK

An experimental investigation into the fluctuating pressure acting on sediment particles on the bed of an open-channel flow was carried out in a large laboratory flume for a range of flow depths and bed slopes. The pressure measurements were made using 23 spherical particles instrumented with differential pressure sensors. These measurements were complemented with simultaneous measurements of the velocity field using high-resolution stereoscopic particle image velocimetry. The pressure statistics show that the standard deviations of the drag and lift fluctuations vary from 2.0 to 2.6 and from 2.5 to 3.4 times the wall shear stress, respectively, and are dependent on relative submergence and flow Reynolds number. The skewness is positive for the drag fluctuations and negative for the lift fluctuations. The kurtosis values of both drag and lift fluctuations increase with particle submergence. The two-particle correlation between drag and lift fluctuations is found to be relatively weak compared to the two-point drag–drag and lift–lift correlations. The pressure cross-correlations between particles separated in the longitudinal direction exhibit maxima at certain time delays corresponding to the convection velocities varying from 0.64 to 0.72 times the bulk flow velocity, being very close to the near-bed eddy convection velocities. The temporal autocorrelation of drag fluctuations decays much faster than that for the lift fluctuations; as a result, the temporal scales of lift fluctuations are 3–6 times that of drag fluctuations. The spatial and temporal scales of both drag and lift fluctuations show dependence on flow depth and bed slope. The spectral behaviour of both drag and lift fluctuations is also assessed. A $f^{-11/3}$ slope is observed for the spectra of the drag fluctuations over the majority of the frequency range, whereas the lift spectra suggest two scaling ranges, following a $f^{-11/3}$ slope at high frequencies and $f^{-5/3}$ behaviour at lower frequencies.

**Key words:** channel flow, sediment transport, turbulent flows

---

## 1. Introduction

Knowledge of sediment transport is important for predicting the impact of human intervention in river and coastal systems. Despite the fact that sediment transport

† Present address: Silixa Ltd, Silixa House, 230 Centennial Park, Centennial Avenue, Elstree WD6 3SN, UK. Email address for correspondence: mohammad.amir@silixa.com

has been studied for over a century now, many questions about the mechanisms responsible for entrainment of individual particles and overall erosion remain unanswered. The interaction of sediment particles with the local hydrodynamics is important also for offshore engineering applications. This is testified, among others, by the recent work of Mattioli *et al.* (2012). Predicting the initiation of sediment particles requires a relation linking particle entrainment and the motion of the fluid. Specifically, instantaneous drag and lift forces acting on a particle need to be expressed in terms of flow parameters. If the local flow structure produces a high pressure below the sediment particle, and low pressure above it, a high-lift event will occur. Raudkivi (1990) assumed that sediment particles could be entrained by this mechanism. A high-drag event will occur if there is a high pressure upstream of the particle and low pressure downstream of it. Therefore, indicators of drag and lift events can be obtained by measuring the pressure above and below, and upstream and downstream, of a sediment particle.

Several investigators have attempted to make direct measurements of lift and drag forces on bed particles (e.g. Einstein & El-Samni 1949; Chepil 1958, 1961; Coleman 1967; Coleman & Ellis 1976). Despite their importance to improve understanding of the mechanisms of sediment entrainment, direct measurements of instantaneous forces or pressures acting on sediment particles remain elusive owing to the experimental difficulties involved (Hofland, Battjes & Booij 2005; Detert, Weitbrecht & Jirka 2010*a*). An attempt was made to overcome these difficulties by Schmeeckle, Nelson & Shreve (2007), who conducted force measurements on natural and spherical particles and reported that the instantaneous drag force cannot be accurately predicted from the instantaneous local flow velocity using a constant drag coefficient, even though this method works well for the mean drag force. Instantaneous lift force, on the other hand, is not correlated at all with the streamwise or vertical components of near-bed velocity according to the same study.

Dwivedi, Melville & Shamseldin (2010) experimentally studied the relationship between coherent flow structures and the hydrodynamic forces leading to entrainment of spherical particles in turbulent open-channel flow. In their tests, the hydrodynamic forces on an instrumented sphere with different protrusions and the turbulent flow field were measured simultaneously, and their results showed that the high lift forces that cause particle entrainment are correlated with sweep structures. Using particle image velocimetry (PIV) and the related particle tracking velocimetry (PTV), Van Hout (2013) studied resuspension and saltation of nearly neutrally buoyant polystyrene beads in a turbulent boundary layer. Two sets of experiments, the first on resuspension and the second on saltation, showed that in all cases lift-off coincided with the passage of a vortex core, creating an ejection–sweep cycle (burst) responsible for lift-off. Diplas *et al.* (2008) demonstrated that, in addition to the magnitude of the instantaneous forces applied on a sediment grain, the duration of these forces is also important in determining the sediment grain's threshold of motion, and that their product, or impulse, is better suited for specifying such conditions. The models incorporating this effect therefore require knowledge of the instantaneous local forces acting on the grains. The turbulent flow field at a particular location and the resulting forces are affected by the upstream and local bed structure (Nelson *et al.* 1995; Hofland *et al.* 2005).

More generally, regions of flow separation are often considered as one of the main contributors to the extreme pressures acting on the sediment particles. These flow regions are highly complex and three-dimensional, and the pressure distribution across individual particles can vary greatly. Any such spatial heterogeneity in the pressure

field around a particle can induce strong lift and drag forces, which in turn can induce sediment motion. Therefore, understanding bed pressure fluctuations is important for predicting the likely onset of entrainment.

More recently, Chan-Braun, Villalba & Uhlmann (2011) carried out direct numerical simulation (DNS) of turbulent open-channel flow at low Reynolds numbers. Two sizes of spherical particles were considered in their study. In the first case, the spheres were small and the limit of the hydraulically smooth flow regime was approached. In the second case, the spheres were more than three times larger and the flow was in the transitionally rough flow regime. For both cases they found that the main contributions to the overall drag, lift and spanwise torque came from the surface of the upper part of the particle. The amplitude of the particle force fluctuations was found to be significantly larger in the large-sphere case (i.e. at larger particle Reynolds number), while the trend differs for the fluctuations of the individual components of the torque.

Early experimental work on pressure measurements in turbulent boundary layers is summarised in the review papers of Willmarth (1975) and Ecklemann (1988). One of the initial studies to note was by Willmarth & Wooldridge (1962), who reported a comprehensive set of measurements of the fluctuating pressure at the wall beneath a thick boundary layer. Their experiments were conducted over smooth and continuous (i.e. impermeable) rough surfaces. They found that the spatial extent of correlation of fluctuating pressures is approximately the same in directions along and transverse to the flow. Willmarth & Wooldridge (1962) also revealed that pressure disturbances associated with larger eddies travelled downstream faster than those associated with smaller eddies, with the convection velocities ranging from 56 to 83 % of the free-stream velocity. One of the major findings from their study was that the standard deviation of the wall pressure, $\sigma_p$, was 2.19 times the wall shear stress, $\tau_0$. Willmarth & Roos (1965) made measurements of the wall pressure in a boundary layer over a flat surface and found that $\sigma_p/\tau_0 = 2.66$. Blake (1970) obtained an average value of $\sigma_p/\tau_0 = 3.4$ for different rough walls, with actual values varying between 2.9 and 3.8 depending on roughness type and magnitude. As a reasonable average from the experimental data of various authors, Hinze (1975) suggested $\sigma_p \approx 3\tau_0$ and that this ratio is Reynolds-number dependent. Farabee & Casarella (1991) analysed a dataset from numerous studies of direct wall pressure measurements and found a weak increase of the values $\sigma_p/\tau_0$ with Reynolds number. Smart & Habersack (2007) measured near-bed, sub-bed and uplift pressure fluctuations in gravel-bed rivers and found that the standard deviation of near-bed pressure fluctuations was approximately three times the local time-averaged bed shear stress, and also that the pressure structures in the flow decayed rapidly.

The river and open-channel flume measurements of Smart (2005, 2008) indicate a direct link between pressure fluctuations within the surface layer of a river bed and the onset of sediment movement. Hofland *et al.* (2005) made measurements of pressures and simultaneous near-bed velocities in a flume roughened with crushed stones. Three pressure transducers were placed in a 30 mm cube made of stainless steel that was part of the granular bed. The magnitude of the fluctuating pressure was revealed to increase with the exposure relative to the stones upstream of the cube. Drag caused by longitudinal velocity fluctuations was seen as the source of the largest force fluctuations for the most exposed stone. However, this clear force origin weakened with subsiding exposure effects. Detert (2008) and Detert *et al.* (2010*a*) carried out experiments to describe the statistical properties of fluctuating pressure in and above different granular porous beds. They found two simplified equations that describe the downward decrease of the standard deviation of the measured fluctuations

indicating drag and lift, respectively. The former relation is given by a crude linear fit, whereas the latter shows that the lift fluctuations decrease downwards exponentially in the porous bed. Within the subsurface layer, the standard deviation reaches a non-zero constant, mainly dominated by long-wave pressure fields that are convected in the outer flow.

The studies reported so far have mainly focused on fluctuating pressure over smooth beds and continuous (impermeable) rough beds. Far fewer studies over discontinuous (granular) rough beds have been carried out, especially at high particle and global Reynolds numbers in open-channel flows. Because of the computational limitations, numerical studies of open-channel flows have mainly been restricted to lower-Reynolds-number regimes (Singh, Sandham & Williams 2007; Chan-Braun *et al.* 2011). Apart from Detert (2008), there is no account of any other experimental work that involves simultaneous measurements of fluctuating pressure on multiple bed particles, particularly covering a wide range of spatial separations along and across the flow. These types of measurements are essential for developing a better understanding of the instantaneous force components whose origin is the pressure gradients (Einstein & El-Samni 1949; Schmeeckle *et al.* 2007). This information will help to understand the occurrence of physical processes both upstream and downstream of the initial point of sediment entrainment. It is also equally important to understand the effects of relative submergence and bed slope on the forces acting on the particles in the bed in order to build more accurate predictive models.

The main goal of the present work is to provide new information on spatial and temporal structure of fluctuating pressure acting on a rough granular bed in turbulent open-channel flow at high particle and global Reynolds numbers, as well as to identify and quantify the effects of relative flow submergence and bed slope. In order to achieve this, differential pressure measurements have been made under a range of hydraulic conditions by a large array of 23 sensors incorporated within the bed of an open-channel flow. These pressure measurements were supplemented with simultaneous measurements of the overlying velocity field using stereoscopic PIV.

Following this introduction, details of the experimental set-up and all equipment are described in § 2. A summary of the hydraulic conditions that were investigated is given in § 3 along with a brief discussion of associated measurement uncertainties. Background flow velocity statistics from PIV data are provided in § 4, and the analysis of the differential pressure measurements is reported in § 5. The paper finishes with a brief set of conclusions in § 6.

## 2. Experimental set-up

Experiments were conducted in a open-channel flow. PIV was used to measure the velocity field, while an array of differential pressure sensors were employed to make multi-point pressure measurements on the sediment particles. A standard experiment included the synchronous measurements of velocity, pressure at multiple particles and water surface elevation for a total duration of 10 min. Each standard experiment was repeated under a number of different hydraulic conditions. Since this study deals with fixed-bed flows, the hydraulic conditions employed were chosen so that the bed shear stress would be less than the critical value required to entrain the glass particles used in our experiments. The Shields criterion (Shields 1936) was used to calculate this critical value. An outline of the experimental facility and equipment used is given in the following sections.

## 2.1. *Aberdeen Open-Channel Facility*

Experiments were carried out using the Aberdeen Open-Channel Facility (AOCF). The AOCF comprises three main components: an open-channel flume, an instrumental carriage and an advanced modular PIV system. The recirculating flume has a working length of 18 m and is 1.18 m wide. The pumps are capable of delivering flow rates up to 150 l s$^{-1}$. The bed slope is adjustable over a range of 3° using a system of automatic jacks. Both the pumps and jacks are computer-controlled, allowing accurate establishment of the desired flow conditions. A combination of aluminium honeycomb mesh and vertical vanes, made from stainless steel, are positioned in the entrance tank to straighten and condition the flow. Backwater profiles are controlled by a weir consisting of 12 vertical metal vanes. The opening of the vanes, which in turn moderates the water surface profile, is accurately measured by a laser displacement meter (LC-2400 by Keyence), thus enhancing the repeatability of a particular flow set-up. An instrumental carriage runs along the length of the flume on rails attached to the top of the side walls and carries instrumentation for measuring bed and water surface elevations, data-logging equipment and a PIV system (computers, laser, optics, etc.). The carriage is motorised and is controlled by a central personal computer (PC), thus offering accurate positioning (within ±1 mm) at any convenient location along the length of the flume. The flow rate is measured using an electromagnetic flow meter located in the discharge pipe prior to the flume entrance. Three ultrasonic range finders (URFs), two Baumer (UNAM 12U9914/S14) and one Banner (U-GAGES18U), were used for various bed and water surface profiling.

## 2.2. *Granular bed*

The granular bed comprised one layer of fixed spheres in a hexagonally close-packed pattern, which covered the whole flume bed. The spheres are made of transparent glass and are 16 mm in diameter with a tolerance of ±0.25 mm. Perforated stainless-steel plates (2 mm thick), which are screwed to the bed, hold the spheres in place ensuring highly regular hexagonal packing along the length of the flume. Black glass marbles with a finer tolerance of ±0.127 mm were placed instead of the transparent marbles over the PIV measurement area in order to minimise laser light scattering.

## 2.3. *Pressure sensors*

Point measurements of differential pressure on the sediment particles were made using Honeywell piezo-resistive sensors (24PCE series). The sensors have a full-scale range of 3450 Pa. Each pressure sensor has a high-pressure port (voltage increases with increasing pressure) and a low-pressure port (voltage decreases with increasing pressure). The diameters of the high- and low-pressure ports are 1 mm and 1.5 mm, respectively, and their depths are 8 mm and 6.5 mm, respectively. A connecting tube between a measurement point and the pressure-sensing element is a common part of pressure measurement systems. Dynamic characteristics of the resulting fluid oscillator may significantly influence the magnitudes of dynamic measurement errors. The dynamic characteristics of pressure measurement systems including connecting tubes have been studied by various authors (see Irwin, Cooper & Girard 1979; Yoshida, Tamura & Kurita 2001). More recently, Bajsic, Kutin & Zagar (2007) examined the dynamic characteristics of connecting tubes of different lengths and diameters by studying the response time to a step change of the input pressure. Their results showed that pressure tubes of short length and internal diameter should be chosen to achieve
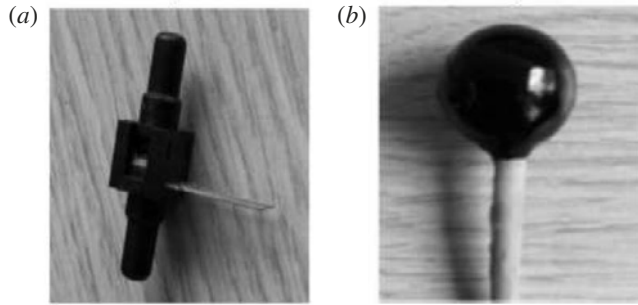
FIGURE 1. (*a*) Original pressure sensor and (*b*) instrumented particle with pressure sensor inside the spherical particle (not to scale).

the fastest response times. Based on these studies, the small diameter and length of the pressure sensors used in the present study should therefore provide fast response times (of up to 1 ms) and keep the dynamic errors to a minimum. In addition to this, we also chose 24PCE pressure sensors, as they are small in size, can be made water resistant and could easily fit inside the spherical particles used in our experiments. However, in order for the sensors to be incorporated within the bed particles, they had first to undergo some modification. More specifically, the cylindrical pressure ports were machined down, and following this the modified sensors were fitted inside two hollow plastic hemispheres, representing an instrumented particle (see figure 1). The particles were then configured in one of two orientations. In the first orientation, the pressure ports were aligned with the flow in order to measure pressure fluctuations representing the drag force. In the second orientation, the ports were aligned perpendicular to the bed to measure pressure fluctuations representing the lift force. As, in turbulent flow, the particle lift and drag forces are due to pressure differences across the particles, the measured differential pressures between the front and back, and between the top and bottom, of the particles relate to drag and lift forces, respectively. Several studies provide experimental support to the four-point pressure measurement strategy (e.g. Schmeeckle *et al.* 2007; Detert *et al.* 2010*a*; Dwivedi *et al.* 2010; Celik, Diplas & Dancey 2014). Of course, such data should be treated cautiously and considered as a realistic surrogate of actual drag and lift forces acting on the entire surface of the particles.

To minimise flow disturbance associated with the pressure sensors, it was decided to pass the wiring directly through the flume bed. Lift and drag sensors were accommodated differently. The drag sensor wiring passed simply straight down through the bed. However, owing to the awkward positioning of the lift sensor wiring, it was necessary to keep a straight length of wire before gradually passing it through the bed. This was done with the use of two hollow spheres, which were positioned adjacent to the lift sensor to provide a 'tunnel' for the wiring (see figure 2). Extreme care was taken during the installation process so that the sensors did not move during the experiments. This was done by tightening the cable glands located under the flume. Also, when installing the sensors, the neighbouring particles were removed from the test section to allow easy access to accurately place the instrumented particles without any interference. The surrounding glass particles were then put back when all the sensors had been carefully installed. When installing the drag sensors, straight lines (in the direction of the flow) were marked on the perforated plates
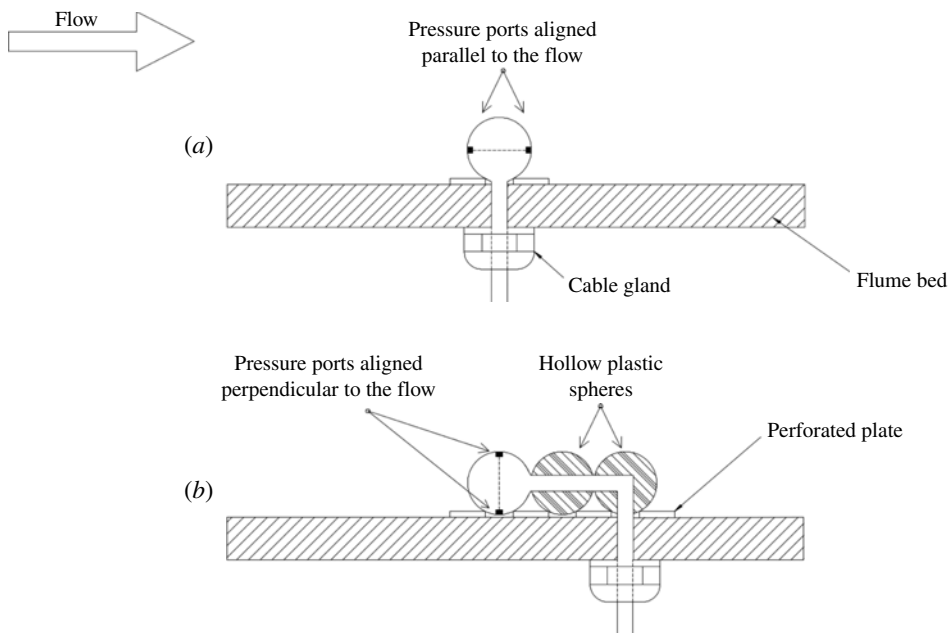
FIGURE 2. Schematic to show (*a*) the drag and (*b*) the lift configurations of the pressure sensors and the passage of their associated wiring through the flume bed.

using waterproof markers so that the pressure ports were aligned relative to these lines. When viewed from the top, the line seemed to bisect the pressure ports of the drag sensor. However, installing the lift sensor with high precision was trickier. It was down to visual inspection of the lift sensors such that, when viewed from the top, the pressure port was directly on top of the particle rather than skewed in any direction. The positions of the pressure ports were examined before and after the experiments to ensure that the sensors remained unchanged during the duration of the experiments.

A total of 23 pressure sensors were used in this study, 16 of which were drag sensors and seven were lift sensors. Their arrangement is shown in figure 3. The pressure sensors were installed over a length of 250 mm and a width 192 mm, i.e. the length and width were intermittently covered. In the longitudinal direction, the spacing between the drag sensors was 27.7 mm, while in the transverse direction, the spacing was 32 mm. This particular arrangement covers a wide area, thus enabling the investigation of spatial correlation between drag–drag, drag–lift and lift–lift pressure sensors, including relevant time and length scales. In order to detect a spatial correlation, it was intended to keep the spacing between the neighbouring sensors to a minimum in both directions. In the transverse direction, this spacing was limited by the presence of the cable glands (see figure 2), which prevented the sensors from being installed side by side across the flow. However, in the longitudinal direction, the drag sensors were installed along the centreline of the measurement section with a minimum spacing.

The centre of the measurement section is indicated by position 1 in figure 3. Upstream of position 1, the distance will be indicated as negative (i.e. '$-x$') and downstream it will be indicated as positive ('$+x$'). Similarly, the right-hand side of position 1 will be indicated as negative ('$-y$'), with the opposite direction being
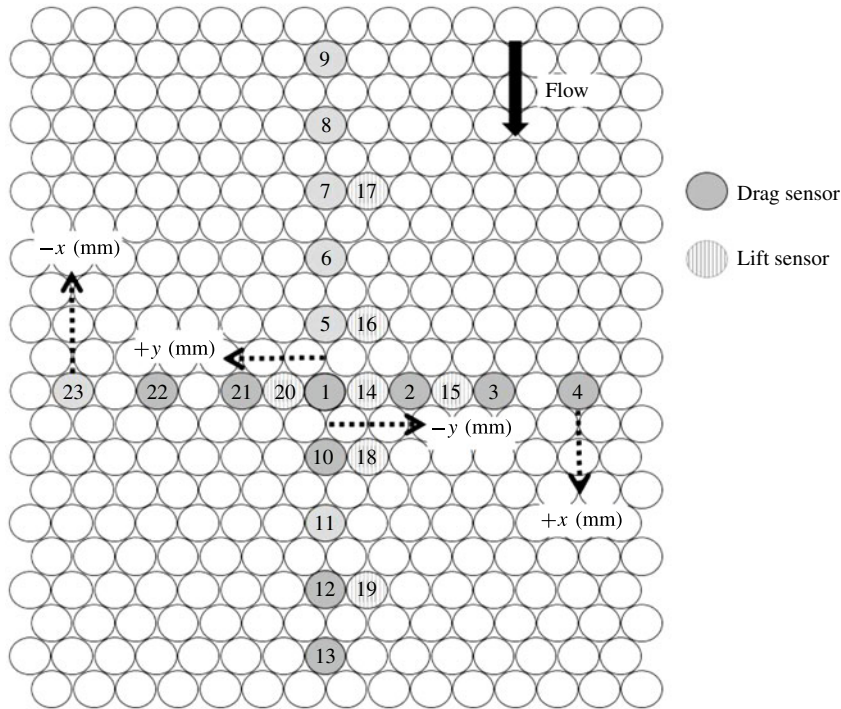
FIGURE 3. Plan view to show the arrangement of the pressure sensors on the flume bed.

positive ('+y'), as shown in figure 3. Therefore, in all the considerations below, position 1 will be referred to as $(x, y) = (0, 0)$.

The pressure sensors were connected to input/output (I/O) modules (National Instruments NI 9237 C Series). Each module can hold four pressure sensors and there are six modules in total. The NI 9237 modules contain all the signal conditioning required to power and measure up to four sensors. These modules are housed in a chassis (NI cDAQ-9178). The cDAQ device manages data transfer between the I/O modules and the PC and also controls triggering and synchronisation of the pressure sensors. The NI cDAQ chassis is itself connected via a universal serial bus (USB) to a desktop PC, and acquisition of pressure data was made using the software LabView Signal Express.

Static calibration of the instrumented particles was performed over a range of 0–15 cm of water column by measuring the output voltage of each pressure sensor to various water levels inside a specially designed calibration device. Calibration coefficients were determined for each sensor and used to convert the output voltages into differential pressures. The calibration device allowed the calibration of each pressure port (of one sensor) separately, revealing two coefficients, which were within $\pm 1\,\%$ for all sensors. The static calibration device is shown in figure 4. The sensors were attached in the central wall such that one pressure port faced the right tank and the other faced the left tank. Using the tap valve, an equilibrium state (equal water levels in each tank) was achieved in the device first. Water was then poured at regular height intervals into one tank while the level of water in the other tank remained constant. This process allowed calibration of one pressure port at a time. Figure 5 shows the calibration data for both parts of one sensor, and as expected

FIGURE 4. (Colour online) Static calibration device.

they exhibit a linear response. The calibration coefficients of the two pressure ports for this sensor are within $\pm 0.5\%$. The sensors also exhibit an initial (zero differential pressure) offset voltage, which changes with a change in ambient conditions. The calibration plots in figure 5 may suggest that the offset voltage is different for each pressure port, but this is not the case. A difference in the offset voltage is observed because each calibration was performed at different times during which the offset voltage decreased from 0.3406 to 0.3019 mV.

Dynamic performance of the instrumented particles was evaluated using a lightweight nylon spherical particle in the running flume. The nylon particle was released upstream of the measurement section to generate pressure changes by coming into contact with the bed. As this particle hits the bed, a peak is generated in the output signal of the pressure sensor. Upon close examination of this signal, we see that the amplitude of the pressure damps out with time as seen in figure 6(*a*). The damping time characterises the temporal response of the pressure sensor. The frequency content of this signal was evaluated using fast Fourier transform (FFT) to identify the natural frequency of the pressure sensor. The power spectral density (PSD) shown in figure 6(*b*) exhibits a flat response up to approximately 120 Hz and also shows a sharp peak at approximately 400 Hz that corresponds to the natural frequency of the sensor. All drag and lift sensors were tested in this way, and their natural frequencies varied between 380 and 420 Hz, with a flat response of up to at least 120 Hz. Taking into account that in our experiments most of the energy of velocity fluctuations and associated pressure fluctuations are within this frequency range, the results in figure 6 suggest that our sensors provide fairly accurate estimates of pressure statistics.
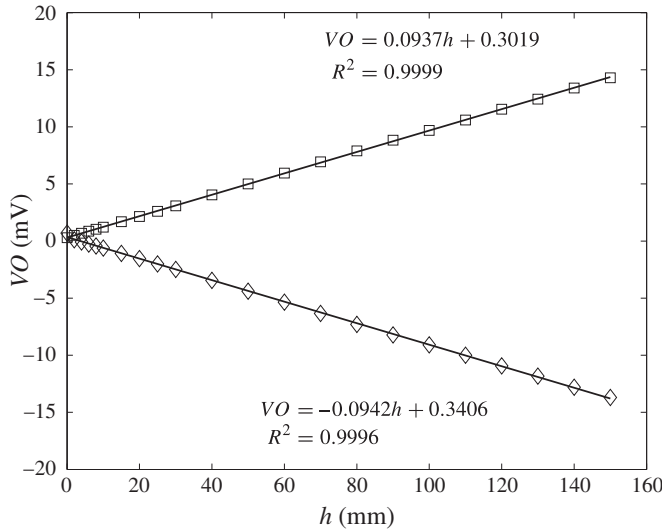
FIGURE 5. Voltage output *VO* of the sensor against water height *h*. The solid lines represent the linear best fit through the data points for each pressure port: positive port (□); negative port (◇). The equations of each line are also shown.
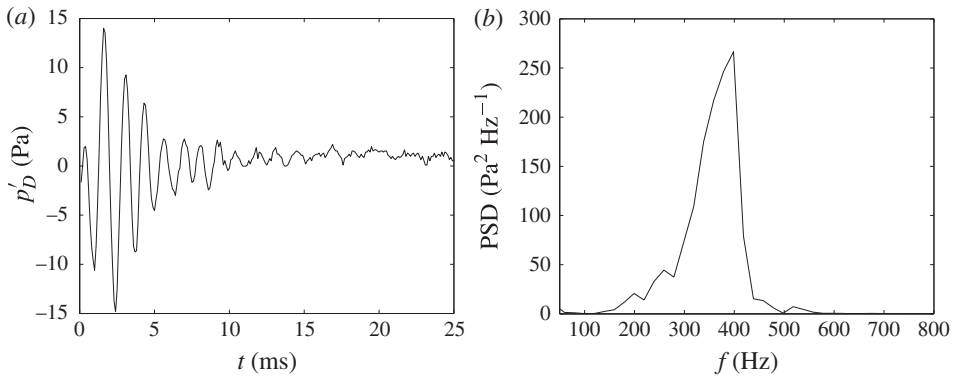


FIGURE 6. (*a*) Response of pressure sensor upon particle impact with the bed and (*b*) PSD against frequency of pressure sensor. Drag sensor 5 used as an example.

As mentioned earlier, the pressure sensors exhibited an initial (zero differential pressure) offset voltage, which changed from time to time due to potential changes in ambient conditions. Because of this, all pressure data presented in this study were detrended (i.e. the mean value was removed) and therefore the main focus in the paper is on the fluctuating pressures, i.e. pressure deviations from the mean values.

### 2.4. *The particle image velocimetry system*

The Aberdeen PIV system has been developed in-house at the University of Aberdeen by Dr Stuart Cameron (Cameron 2011; Cameron *et al.* 2013). The system comprises four cameras (DALSA 4M60, complementary metal oxide semiconductor sensor, 2352 pixel × 1728 pixel resolution at 62 frames per second (f.p.s.)) with
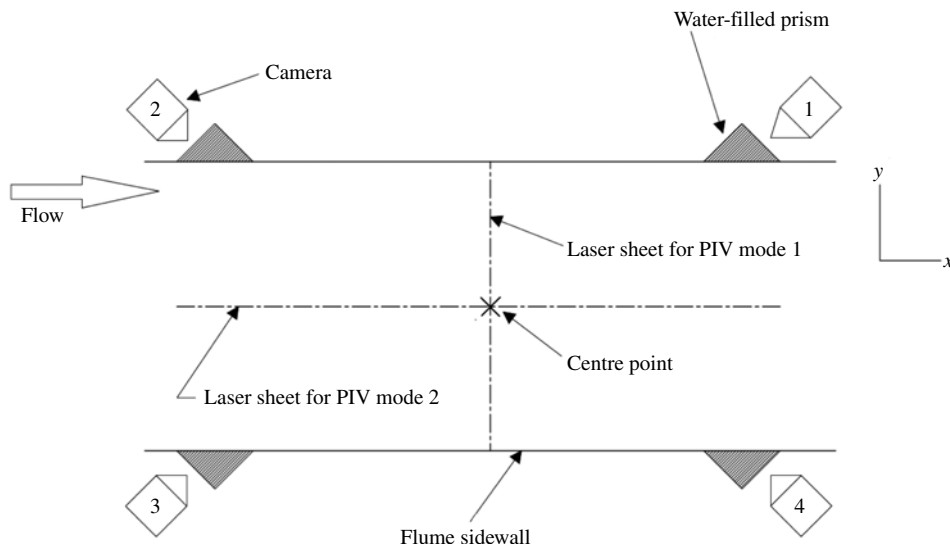
FIGURE 7. Plan view of PIV layout for modes 1 and 2 (not to scale).

adjustable Scheimpflug mounts that allow non-orthogonal viewing of the light-sheet plane. Laser light is provided by twin neodymium-doped yttrium aluminium garnet (Nd:YAG) lasers (Oxford Lasers Neo 50-100/100-50 PIV) set to operate in a pulsed mode. Silver-coated hollow glass spheres (20–32 µm in diameter, 0.8–1.0 g cm$^{-3}$, Isospheres) are used as PIV flow tracers.

Two modes of stereoscopic PIV were employed in the current study with the cameras arranged in an angular displacement configuration (Prasad 2000) and the light sheet oriented to permit measurement of the flow field in a transverse–wall-normal ($y$–$z$) plane across the centre of the channel (referred to as PIV mode 1) and a longitudinal–wall-normal ($x$–$z$) plane along the centre of the channel (referred to as PIV mode 2) as shown in figure 7. For both modes, the cameras viewed the measurement plane through water-filled glass prisms that were attached to the flume sidewall to minimise distortions caused by the air–glass–water interface (Prasad 2000). Each camera was used to estimate a two-component velocity field. Prior to cross-correlation analysis, the two-component field was first 'dewarped' onto a grid with constant magnification following the mapping method of Willert (1997). The calibration procedure to obtain the mapping function necessary to perform the transformation is described in detail in Cameron *et al.* (2013). The benefit of having four camera measurements was that each different camera pair could be used to obtain independent estimates of each velocity component. This feature has recently been exploited by Cameron *et al.* (2013), wherein the authors demonstrate how to calculate significantly noise-reduced statistics from two-camera stereoscopic PIV data in the field. A near-identical procedure was adopted here, except that the extension was made to four-camera measurements. All velocity processing was carried out using custom software written and developed at the University of Aberdeen, further details of which may be found in Cameron (2011) and Cameron *et al.* (2013). The software employs an iterative deformation algorithm with Fourier-transform-based cross-correlation. The general steps required to implement this particular class of algorithm is discussed further in Cameron (2011). However, several features that are specific to the present

algorithm have to be mentioned. Firstly, image interpolation was carried out during each iteration using a 10 pixel × 10 pixel sinc kernel, weighted with a Blackman window. Secondly, the interrogation regions were fixed at 64 pixel × 64 pixel and were weighted with a Blackman window. Finally, the scale factor of the 'dewarped' images was set at 10 pixel mm$^{-1}$, which, alongside the chosen overlap in interrogation regions, yielded a vector grid spacing of 1 mm.

## 2.5. *Synchronisation and data recording settings*

A six-channel transistor–transistor logic (TTL) signal generator (R&D Vision) controlled the timing of the entire system and allowed synchronous measurements of PIV velocity, pressure and water surface elevation. Channels 1–4 control the timing of both the flash-lamp and Q-switch of lasers 1 and 2; a four-way TTL splitter is connected to channel 5 to allow simultaneous connection to all four cameras; channel 6 provides a digital trigger to the NI cDAQ 9178, which in turn then controls the acquisition of the pressure sensor data. The flow rate was measured independently throughout the duration of the experiments. The sampling frequencies of the PIV were 32, 50 and 80 Hz for flow depths of 120, 80 and 40 mm, respectively. The sampling frequencies of the PIV were determined mainly by limitations in the recording capabilities of the cameras. At maximum resolution (i.e. when the field of view of the camera is 2352 pixel × 1728 pixel), the frame rate of the cameras is 60 f.p.s., which limits the sampling frequency to $60/2 = 30$ Hz at full resolution. The field of view of the camera was in turn set according to the flow depth. Therefore, the deep flows ($H = 120$ mm) had the lowest sampling frequencies since they required a larger field of view. As the depth decreased, fewer pixels were needed to cover the flow depth, so the cameras were capable of recording at a higher sampling frequency. In all cases, the aim was to maximise the sampling rate for the given measurement window, which for both PIV modes had height $= H$ and length $= 30$ cm. For pressure measurements, all recordings were made at a sampling frequency of 10 kHz with a view to future filtering of the data. The pressure sensor time-series data can be easily down-sampled to match the sampling frequency of the velocity time-series data from PIV. However, owing to the finite time that the digital trigger takes to activate the pressure sensor data acquisition, a small but non-negligible time delay exists between the pressure data and the velocity data. The exact time delay was measured in separate tests and found in all cases to be of the order of 2.5 ms. The measurement duration was fixed in each experiment at 10 min, which was more than two orders of magnitude longer than the time scale of the largest turbulent structures present in the studied flows. Also, the measurement duration was set to 10 min as a compromise between collecting an adequate number of samples for statistical estimates and available data storage capacity. A complementary study of Stewart (2014) showed that 10 min duration provides fairly high accuracy for bulk velocity statistics up to the fourth order.

The data from PIV mode 1 are used to characterise background flow structure in § 4 while the data from PIV mode 2 are employed to extract information on eddy convection velocities to compare them with pressure convection velocities in § 5.2.2.

## 3. Flow configurations and measurement uncertainties

A total of nine steady and uniform flow scenarios were tested as summarised in table 1. In the table, $S_b$ is the bed slope, $H$ denotes the flow depth (measured from the particle tops to the water surface), $U_b = Q/A$ is the bulk mean velocity (where $Q$

| Run nos | $S_b$ | $H$ (mm) | $U_b$ (m s$^{-1}$) | $Re_b$ | $Fr$ | $B/H$ | $H/D$ | $u_{*s}$ (m s$^{-1}$) | $u_{*uw}$ (m s$^{-1}$) | $Re_*$ | $Re_p$ |
|---|---|---|---|---|---|---|---|---|---|---|---|
| 1 | 0.0003 | 40 | 0.122 | 4 915 | 0.19 | 29.5 | 2.5 | 0.0109 | 0.0106 | 427 | 170 |
| 2 | 0.0015 | 40 | 0.264 | 10 678 | 0.42 | 29.5 | 2.5 | 0.0244 | 0.0235 | 949 | 376 |
| 3 | 0.003 | 40 | 0.369 | 14 831 | 0.59 | 29.5 | 2.5 | 0.0344 | 0.0336 | 1347 | 538 |
| 4 | 0.0003 | 80 | 0.194 | 15 508 | 0.22 | 14.8 | 5.0 | 0.0153 | 0.0152 | 1213 | 243 |
| 5 | 0.0015 | 80 | 0.400 | 32 373 | 0.45 | 14.8 | 5.0 | 0.0345 | 0.0329 | 2658 | 526 |
| 6 | 0.003 | 80 | 0.566 | 45 763 | 0.64 | 14.8 | 5.0 | 0.0488 | 0.0471 | 3806 | 724 |
| 7 | 0.0003 | 120 | 0.245 | 29 576 | 0.23 | 9.8 | 7.5 | 0.0188 | 0.0187 | 2251 | 299 |
| 8 | 0.0015 | 120 | 0.524 | 63 305 | 0.48 | 9.8 | 7.5 | 0.0421 | 0.0411 | 4961 | 658 |
| 9 | 0.003 | 120 | 0.737 | 88 729 | 0.68 | 9.8 | 7.5 | 0.0595 | 0.0574 | 6911 | 918 |

TABLE 1. Flow configurations.

is the mean flow rate and $A$ is the cross-sectional area of the flow), $Re_b$ $(= U_b H/\nu)$ is the bulk Reynolds number (where $\nu$ is the fluid kinematic viscosity), $Fr$ $(= U_b/\sqrt{gH})$ is the Froude number, $B/H$ is the aspect ratio (where $B$ is the flume width), $H/D$ is the relative submergence (where $D$ is the particle diameter), $u_*$ is the shear velocity estimated here as $u_{*s} = (gHS_b)^{0.5}$ and by extrapolating the total shear stress profile from the water surface to the particle tops ($u_{*uw}$), $Re_*$ $(= u_{*uw}H/\nu)$ is the friction Reynolds number or Karman number and $Re_p$ $(= u_{*uw}D/\nu)$ is the roughness or particle Reynolds number. Although the two estimates of $u_*$ produced close values (table 1), we use $u_{*uw}$ in the next section, as it provides an appropriate scale for normalising turbulence properties in rough-bed flow at low relative submergence as argued by Pokrajac *et al.* (2006).

The nine flow scenarios can be subdivided into three different bed slopes ($S_b = 0.0003$, 0.0015 and 0.003), each of which has been studied at three flow depths: 120, 80 and 40 mm. It can be seen in table 1 that all flows were fully turbulent, with bulk Reynolds number varying from 4915 to a maximum of 88 729. Further, all flows were subcritical, with Froude number ranging between 0.2 and 0.7. Bulk mean velocity varied from a minimum of 0.122 m s$^{-1}$ for run 1 to a maximum of 0.737 m s$^{-1}$ for run 9. All flows are considered low to intermediate submergence with $H/D \leqslant 7.5$. The lowest $Re_p$ value is $\sim$180, which comfortably exceeds the threshold of $\sim$70 to achieve fully rough conditions. Given the high aspect ratios ($B/H \geqslant 10$), two-dimensional flow is expected along the channel centreline according to empirical guidelines (e.g. Nezu & Nakagawa 1993). The measurement section was located at a minimum of $100H$ (for $H = 120$ mm) from the leading edge of the rough bed (i.e. from the flume entrance). Separate tests (Stewart 2014) showed that the flow was already fully developed beyond $75H$ from the leading edge of the roughness. Water surface profiles were measured using the URFs to verify that the flow remained uniform along the length of the channel. The Shields parameter (dimensionless bed shear stress) $\theta$ $(= u_{*uw}^2/g(S_s - 1)D)$ was calculated for each flow regime, where $S_p = \rho_p/\rho_f$ ($\rho_p$ is particle density, $\rho_f$ is fluid density). The values of $\theta$ varied between 0.0005 and 0.0138, being well below the threshold for particle entrainment.

The combined uncertainty in the flow depth is the contribution from uncertainty in identifying the position of the roughness tops (which was estimated to be no greater than 0.1 mm, based on searching for the roughness tops in PIV images) and measurement noise in the URF signal. To assess the magnitude of noise in the URF signal, measurements were made of the distance to a device filled with

stationary water (the standard deviation of an ideal noise-free measurement would have been zero), so the magnitude of the standard deviation of that signal indicated the level of noise. The value was around 0.12 mm and the total uncertainty in $H$ is then $\pm 1.96(\sqrt{0.1^2 + 0.12^2}) = \pm 0.31$ mm. Uncertainty in the bed slope was estimated using a procedure outlined below. First, the URFs, which were attached to the instrumental carriage, were used to record a profile of the elevation of the dry flume bed along the channel centreline. Second, dams (i.e. transverse vertical walls) were installed at the flume exit and entrance and the flume was filled with water. Third, the URFs were used to make a repeat profile, this time of the horizontal water surface elevation, along the length of the flume. Fourth, the measured dry bed elevation was then subtracted from the horizontal water surface elevation (this operation also allowed the removal of any bias in the measurements from potential vertical variations in the rails that support the instrumental carriage as it traverses the flume). Lastly, a linear regression line was fitted to the residual, the gradient of which is the bed slope. Confidence intervals of the gradient of the regression line were then calculated and the corresponding uncertainty in the bed slope was $\pm 7.1\%$, $\pm 1.4\%$ and $\pm 0.7\%$ for bed slopes of 0.0003, 0.0015 and 0.003, respectively. The flow meter is accurate to within $\pm 0.5\%$ of the measured flow rate. Sampling error is expected to be the dominant contributor to uncertainty in measured velocity statistics. Therefore, the moving block bootstrap technique outlined in Garcia, Jackson & Garcia (2006) was used to estimate sampling uncertainties associated with double-averaged streamwise velocity $\langle \overline{u} \rangle$ (refers to averaging in both space and time domains), spatially averaged streamwise velocity variance $\langle \overline{u'u'} \rangle$ (refers to averaging only in space domain) and spatially averaged Reynolds stress $\langle \overline{u'w'} \rangle$ at $\pm 1.2\%$, $\pm 6.7\%$ and $\pm 6.4\%$, respectively. Further details of these double-averaged and spatially averaged variables are provided in §4. The details on double-averaged and spatially averaged hydrodynamic quantities can be found in Nikora *et al.* (2007*a*,*b*). The uncertainty in pressure measurements was estimated using a standard technique (Moffat 1988) assuming a normal probability distribution of the parameter, which generates a symmetrical interval around the mean value of the parameters. Confidence intervals were therefore evaluated using repeated trials of pressure measurements. The uncertainty in the standard deviation, skewness and kurtosis of the pressure measurements was around $\pm 2\%$, $\pm 7.5\%$ and $\pm 5\%$, respectively.

## 4. Background flow characteristics

As a full account on flow structure from multi-mode PIV data in these experiments will be reported in a separate paper, here we only present some background information that may be helpful in pressure data interpretation. Specifically, below, we examine vertical distributions of streamwise velocities, streamwise turbulence intensities, Reynolds stresses, skewness of streamwise and vertical velocities and streamwise eddy convection velocities. The multi-camera stereoscopic PIV measurements provide redundant estimates of velocity. These were used to minimise measurement noise contributions to all bulk velocity statistics shown here following the method outlined in Cameron *et al.* (2013). The results presented in this section were obtained from PIV mode 1 described in §2.4.

In §3, we described the uncertainties in the evaluation of $\langle \overline{u} \rangle$, $\langle \overline{u'u'} \rangle$ and $\langle \overline{u'w'} \rangle$; we now formally define these quantities. Instantaneous fluid velocity can be decomposed as

$$u_i = \langle \overline{u_i} \rangle + \tilde{u}_i + u'_i, \tag{4.1}$$

where $u_i$ is the $i$th velocity vector component (longitudinal $u$, transverse $v$ and vertical $w$), the angle brackets and overbar represent spatial and temporal averages, respectively, the prime represents a temporal fluctuation (i.e. $u' = u - \bar{u}$) and the tilde represents a spatial fluctuation ($\tilde{u} = \bar{u} - \langle \bar{u} \rangle$). The time averaging is performed over all turbulence scales, as usual, while the spatial averaging of the time-averaged quantities is done over a spatial domain, the size of which exceeds the correlation length scales of bed roughness (in our particular case, it well exceeded the spacing between bed particles). Applying the modified Reynolds decomposition (4.1) and the spatial averaging operators and theorems (e.g. Nikora *et al.* 2007*a*,*b*), one can obtain the double-averaged (in time and space) momentum equation convenient for the description of rough-bed flows, particularly in the near-bed region where heterogeneity of the time-averaged flow is high.

Conceptually, the double-averaged equations relate to the time-(ensemble)-averaged equations as the time-averaged equations relate to the Navier–Stokes equation for instantaneous hydrodynamic variables. A comprehensive overview of this methodology, known as double averaging (in time and then space), is provided in Nikora *et al.* (2007*a*,*b*). Here we only show the simplified double-averaged equation for the longitudinal velocity component $u$ for the conditions of our experiments, which for the central part of the flume can be assumed to be steady, two-dimensional and uniform, i.e.

$$gS_b - \frac{1}{\phi}\frac{\partial \phi \langle \overline{u'w'} \rangle}{\partial z} - \frac{1}{\phi}\frac{\partial \phi \langle \tilde{u}\tilde{w} \rangle}{\partial z} + \frac{1}{\phi}\frac{\partial}{\partial z}\phi\left\langle v\,\overline{\frac{\partial u}{\partial z}}\right\rangle$$
$$+ \frac{1}{\rho}\frac{1}{\phi}\frac{1}{V_o}\iint_{S_{int}}\bar{p}n_x\,\mathrm{d}S - \frac{1}{\phi}\frac{1}{V_o}\iint_{S_{int}}v\frac{\partial \bar{u}}{\partial x_j}n_j\,\mathrm{d}S = 0. \qquad (4.2)$$

In (4.2), $g$ is the gravitational acceleration, $S_b$ is the bed slope, $\phi$ is the ratio of the volume of fluid to the total volume of the averaging domain $V_o$ (thin slab parallel to the bed), $\langle \overline{u'w'} \rangle$ is the spatially averaged Reynolds stress, $\langle \tilde{u}\tilde{w} \rangle$ is the form-induced stress (due to potential correlation between time-averaged longitudinal and vertical velocities), $p$ is pressure, $\rho_f$ is fluid density, $n_i$ is an inwardly directed unit vector normal to the bed surface (into the fluid) and $S_{int}$ is the extent of water–bed interface bounded by the averaging domain. The first term on the left-hand side is a forcing term while the second, third and fourth terms represent the effects of Reynolds, form-induced (also known as dispersive) and viscous fluid stresses. The fifth and sixth terms are pressure and viscous drag acting on the roughness elements, respectively. The last two terms in (4.2) appear only for the region below the roughness crests. Our data show that, in the flow region above the roughness crests (studied in this work, see below), the contributions of form-induced and viscous fluid stresses are negligible compared to the Reynolds stress $\langle \overline{u'w'} \rangle$ within most of the flow depth. In other words, for most of the flow depth, gravity is balanced by the turbulent stresses. In this section, we focus on the quantities that are most relevant for characterising the background conditions of the pressure measurements.

Figure 8(*a*) shows vertical distributions of the double-averaged streamwise velocity as a function of $z/D$. The correct choice for the origin of the vertical axis remains an open issue but here is set equal to the roughness tops as was done in studies under similar conditions (e.g. Manes, Pokrajac & McEwan 2007). The streamwise velocity is then seen to vary logarithmically across the core of the flow.

Vertical distributions of spatially averaged streamwise turbulence intensity for all nine runs are shown in figure 8(*b*). These plots are also compared to the
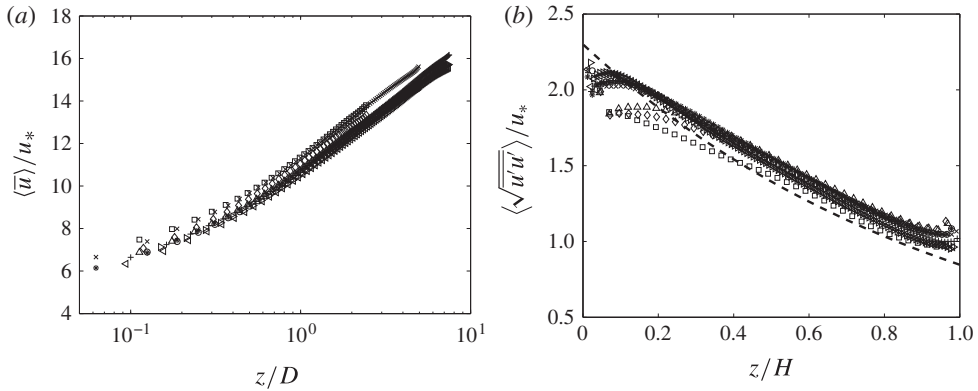
FIGURE 8. (*a*) Double-averaged normalised streamwise velocity as a function of $z/D$ and (*b*) spatially averaged normalised streamwise turbulence intensity as a function of $z/H$. Roughness tops are at $z/D = 0$. Runs: 1 (□); 2 (◇); 3 (△); 4 (×); 5 (∗); 6 (○); 7 (+); 8 (◁); 9 (▷). Dashed line in panel (*b*) is $2.3 \exp(-z/H)$ (Nezu & Nakagawa 1993).

semi-empirical equation of Nezu & Nakagawa (1993) assumed to be valid within $0.1 < z/H < 0.9$ (Nezu 2005). Overall collapse between the profiles is good across the flow depth except at the lowest Reynolds number. The systematic difference between the flows can be observed in the near-bed region just above the roughness tops. This difference appears to be the result of submergence effects, with the peak in streamwise turbulence intensity reducing with decreasing submergence. Similar results have been reported elsewhere (e.g. Lamb, Dietrich & Venditti 2008). However, it may also reflect, to a certain degree, the spatial resolution effect of the PIV, which may lead to suppression of contributions from small-scale velocity fluctuations.

Spatially averaged Reynolds stress distributions are plotted in figure 9 for all nine runs. The Reynolds stress decreases near the bed where viscous and form-induced stresses are likely to increase due to strong velocity gradients and spatial heterogeneities caused by the roughness elements. A similar reduction in the magnitude of the Reynolds stress near the bed is commonly observed in rough-bed open-channel flow (e.g. Cameron 2006; Dwivedi *et al.* 2010). It should be noted, however, that an additional reason for the suppressed Reynolds stress near the roughness tops may also relate to the limited spatial resolution of the PIV configuration used in our measurements. Away from the bed ($z/H > 0.1$–0.2), the normalised profiles demonstrate excellent collapse and closely follow the linear distribution expected for the two-dimensional open-channel flow. These results support the assumption that the flows investigated can be fairly considered as uniform and two-dimensional, in agreement with (4.2).

Spatially averaged skewness distributions for all nine runs are plotted in figure 10. Figure 10(*a*) shows that streamwise velocity skewness $S_u$ is positive at the roughness tops and becomes increasingly negative until it reaches $z/H = 0.7$. Above this location, it starts to reduce its absolute magnitude towards the water surface. In contrast to $S_u$, the vertical velocity skewness $S_w$ remains positive at all wall-normal locations, increasing to a maximum at the water surface (figure 10*b*). Above $z/H = 0.9$, its behaviour becomes difficult to interpret, as it is dominated by a sharp increase in magnitude. This increase is a direct result of normalisation with the vertical velocity variance, which tends rapidly to zero towards the free surface. These profiles are
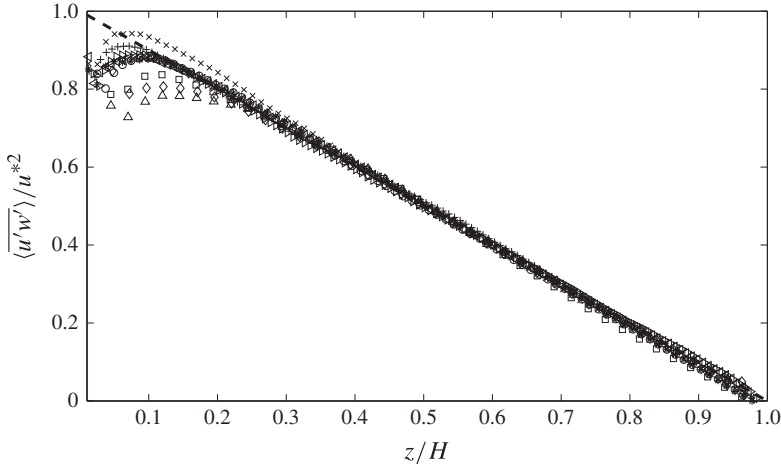
FIGURE 9. Spatially averaged Reynolds stress profiles as a function of $z/H$. Runs: 1 ($\square$); 2 ($\Diamond$); 3 ($\triangle$); 4 ($\times$); 5 ($*$); 6 ($\bigcirc$); 7 ($+$); 8 ($\triangleleft$); 9 ($\triangleright$). Dashed line shows the expected linear distribution for two-dimensional flow.
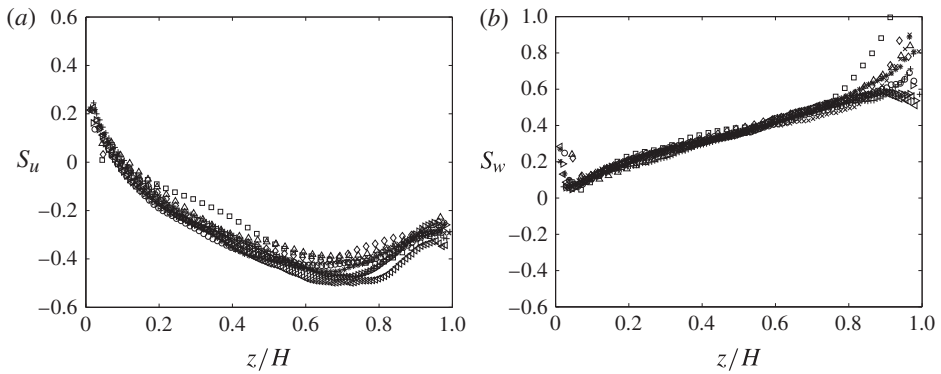


FIGURE 10. Vertical distribution of the spatially averaged skewness coefficients for (*a*) streamwise and (*b*) vertical velocity components. Runs: 1 ($\square$); 2 ($\Diamond$); 3 ($\triangle$); 4 ($\times$); 5 ($*$); 6 ($\bigcirc$); 7 ($+$); 8 ($\triangleleft$); 9 ($\triangleright$).

in agreement with those reported in Cameron (2006) for turbulent rough-bed open-channel flows.

The assessment of the eddy convection velocity is provided in § 5.2.2, where it is compared with the pressure convection velocity. The remainder of the paper now focuses on the results of the differential pressure measurements.

## 5. Pressure fluctuations

### 5.1. *Bulk statistics*

We first examine the bulk statistics of the measured differential pressure, including the standard deviation $\sigma$, skewness $S$ and kurtosis $K$. The standard deviation $\sigma$ of the pressure fluctuations is defined as

$$\sigma^2 = \int_{-\infty}^{\infty} p'^2 P(p') \, \mathrm{d}p' \approx \frac{1}{N} \sum_{i=1}^{N} p_i'^2, \tag{5.1}$$

where $p'$ is the differential pressure fluctuation (deviation from the mean value), $P(p')$ is the probability density function of the differential pressure fluctuation and $N$ is the total number of samples. Skewness and kurtosis describe the asymmetry and peakedness of the pressure distribution, respectively, and are defined as

$$S = \frac{\int_{-\infty}^{\infty} p'^3 P(p')\,\mathrm{d}p'}{\left(\int_{-\infty}^{\infty} p'^2 P(p')\,\mathrm{d}p'\right)^{3/2}} \approx \frac{\left(\dfrac{1}{N}\sum_{i=1}^{N} p_i'^3\right)}{\left(\dfrac{1}{N}\sum_{i=1}^{N} p_i'^2\right)^{3/2}}, \tag{5.2}$$

$$K = \frac{\int_{-\infty}^{\infty} p'^4 P(p')\,\mathrm{d}p'}{\left(\int_{-\infty}^{\infty} p'^2 P(p')\,\mathrm{d}p'\right)^{2}} - 3 \approx \frac{\left(\dfrac{1}{N}\sum_{i=1}^{N} p_i'^4\right)}{\left(\dfrac{1}{N}\sum_{i=1}^{N} p_i'^2\right)^{2}} - 3. \tag{5.3}$$

A value of 3 is subtracted in (5.3) to make the kurtosis of the standard normal distribution equal to 0. Note that, from here onwards, $\sigma$ will also be referred to as $\sigma_D$ or $\sigma_L$, $S$ as $S_D$ or $S_L$, and $K$ as $K_D$ or $K_L$, where the subscripts $D$ and $L$ correspond to the drag and lift fluctuations, respectively.

For each flow condition, the variation in the bulk statistics was investigated in both the longitudinal and transverse directions. Figure 11 shows $\sigma$, $S$ and $K$ as functions of longitudinal and transverse directions for runs 3, 6 and 9 with the bed slope set at 0.003. It can be seen that both $\sigma_D$ and $\sigma_L$ increase with submergence, most likely reflecting increasing streamwise turbulence intensities (as in figure 10b). Figure 11(a,b) shows that $\sigma_D$ at different locations in the longitudinal direction is approximately the same as it is in the transverse direction, indicating that the flow is fairly homogeneous within the measurement section. For each flow condition, spatially averaged values of $\sigma_{D,L}$, $S_{D,L}$ and $K_{D,L}$ were calculated by averaging over all sensors located in either the longitudinal or transverse direction. The spatially averaged value at each flow depth is indicated by a dotted line and for the sake of clarity these lines have been included in figure 11(a–c) only. The spatially averaged value of $\sigma_L$ is higher than the spatially averaged value of $\sigma_D$ at all flow depths. Indeed, the ratio $\sigma_L/\sigma_D$ varies between 1.35 and 1.52. As the lift force is directly proportional to the pressure difference between the top and the bottom of the particle, this result suggests that the extreme values of the lift force experienced by a zero-protrusion spherical particle at all submergences would be greater than those of the drag force. The spatially averaged skewness of drag fluctuations is positive in both the longitudinal and transverse directions. The small positive $S_D$ was also observed by Chan-Braun (2012) in his DNS, supporting a conjecture that high-drag events are more likely compared to low-drag events. For the lift fluctuations, $S_L$ is negative, and increases in magnitude with increasing submergence (figure 11f). This means that large negative lift fluctuations are more likely to occur than large positive lift fluctuations, and this disparity grows with increase in submergence. The kurtosis for both the drag and lift particles increases with submergence as seen in figure 11(g–i), indicating a growing intermittency of the flow as the flow depth increases. Flow intermittency is the tendency of the probability distributions of the drag and lift fluctuations to develop long tails of rare but strong events. With increasing submergence (and flow
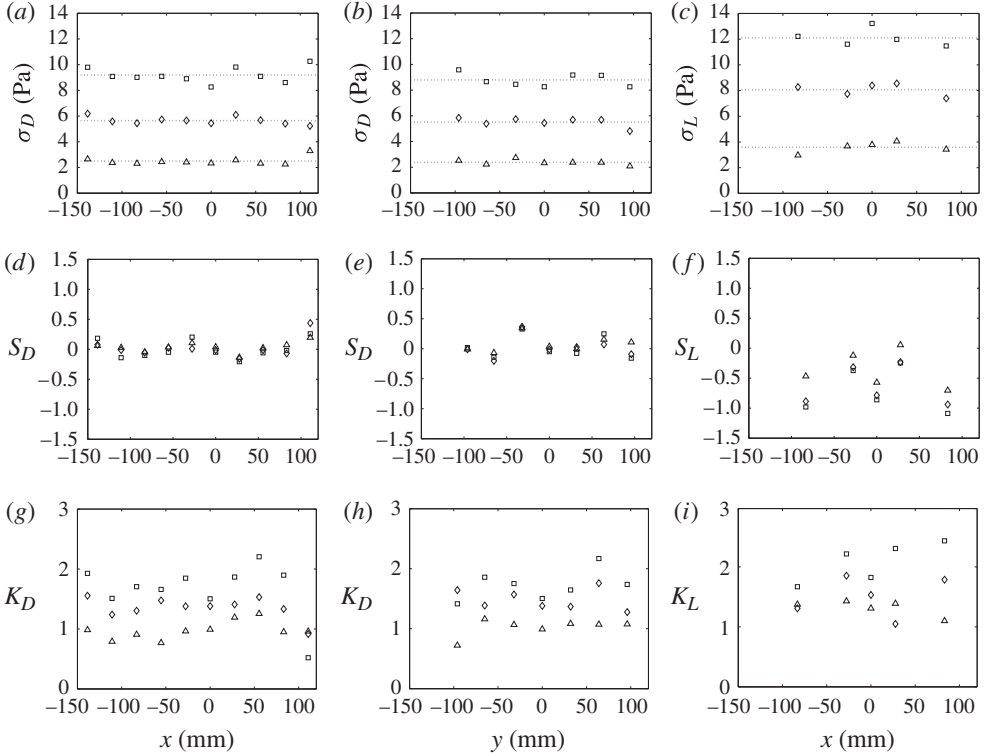
FIGURE 11. Bulk statistics $\sigma$, $S$ and $K$ of pressure fluctuations for runs 3, 6 and 9 depending on the particle location in $(a,d,g)$ the longitudinal direction and $(b,e,h)$ the transverse direction; and $(c,f,i)$ lift pressure fluctuations at different locations in the longitudinal direction. Symbols: $\square$, $H/D = 7.5$; $\diamond$, $H/D = 5.0$; $\triangle$, $H/D = 2.5$.

Reynolds number) the extreme tails become stronger, resulting in higher values of kurtosis as observed by Chan-Braun (2012). Similar trends to those seen in figure 11 were also observed for bed slopes of 0.0015 and 0.0003 (not shown here).

Spatially averaged values of $\sigma$, $S$ and $K$ were obtained for runs 1–9 and these are shown as functions of bed slope in figure 12. It can be seen in figure 12($a,b$) that both $\sigma_D$ and $\sigma_L$ increase fairly linearly with bed slope, the rate of which increases with increasing $H/D$. The lift fluctuations, however, show a steeper increase in $\sigma$ at each $H/D$ than the drag fluctuations. Spatially averaged pressure statistics in the longitudinal and transverse directions are revealed to be very similar in figure 12($a$–$c$), again suggesting that the flow is uniform and homogeneous within the measurement window for all the test cases covered in this study. The coefficient $S_D$ for drag measuring particles is positive and is unaffected by the bed slope as seen in figure 12($c$), while figure 12($d$) shows that, for the lift particles, $S_L$ is negative for all flow cases tested. The results also show that, at a fixed value of $S_b$, the absolute value of $S_L$ becomes larger with increasing $H/D$. However, at a fixed value of $H/D$, little or no dependence of $S_L$ on $S_b$ can be seen. Figure 12($e,f$) shows that, at fixed $S_b$, the kurtosis of both the drag and lift fluctuations increase with increasing submergence. At fixed $H/D$, some dependence of both $K_D$ and $K_L$ on $S_b$ is shown in figure 12($e,f$), although the trends are not consistent for all submergences tested.
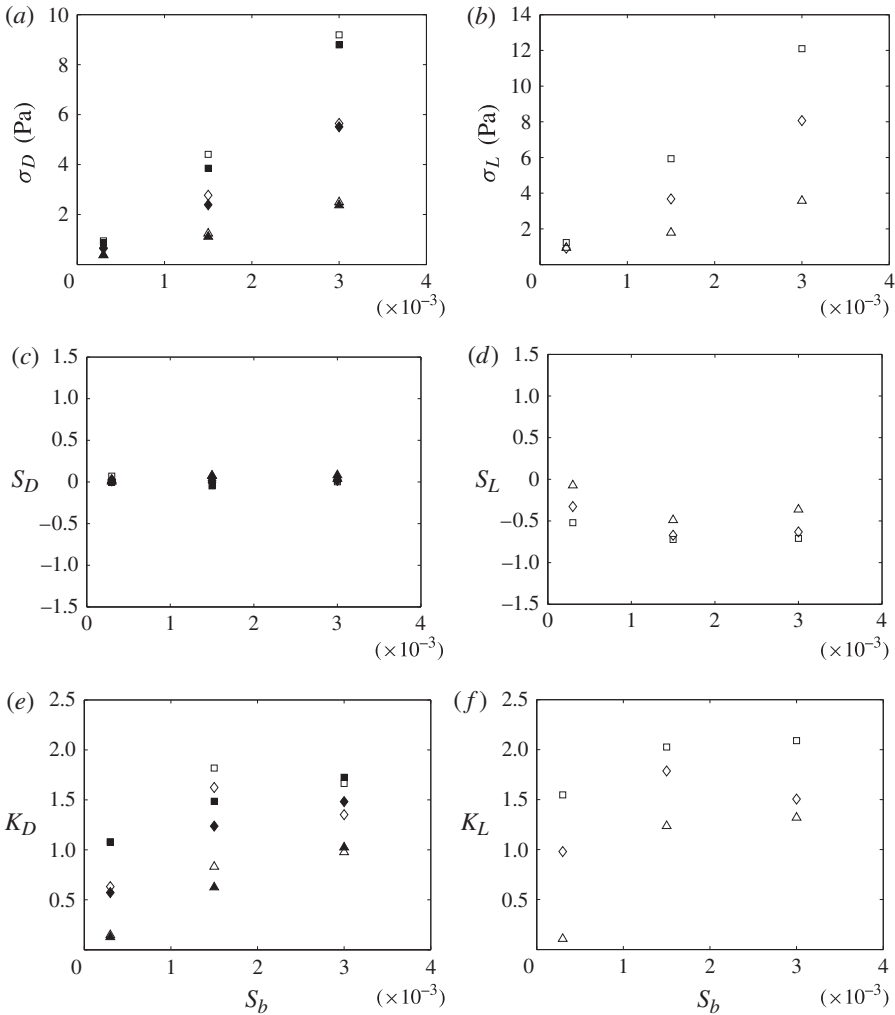
FIGURE 12. Spatially averaged values of $\sigma$, $S$ and $K$ in the longitudinal ($\square$, $\Diamond$, $\triangle$) and transverse ($\blacksquare$, $\blacklozenge$, $\blacktriangle$) directions as a function of $S_b$ for ($a,c,e$) drag and ($b,d,f$) lift fluctuations. Symbols: $\square$, $\blacksquare$, $H/D = 7.5$; $\Diamond$, $\blacklozenge$, $H/D = 5.0$; $\triangle$, $\blacktriangle$, $H/D = 2.5$. For clarity, different scales are used in the vertical axis for panels ($a$) and ($b$).

In general, only the standard deviations of both the lift and drag fluctuations show a linear dependence on both $S_b$ and $H/D$.

  Researchers have long suspected coherent structures to be involved in sediment transport and tried to explain phenomena such as particle uplift from the bed as a result of the existence of these structures. The coherent structures that occur in the near-wall flow region have been extensively reviewed by Kline (1978), Cantwell (1981), Hussain (1986), Robinson (1991), Adrian (2007) and more recently Adrian & Marusic (2012). In the near-wall layer, a sequence of events, more commonly referred to as a burst (or burst cycle), has been observed to occur with ejections and sweeps as its most important phases (Garcia, Nino & Lopez 1996). During the ejection phase, a three-dimensional structure, composed of low-speed fluid, is pushed away from

the bed into the flow, whereas in the sweep phase, high-speed fluid moves down towards the bed, locally spreading sideways. Evidence for such dynamics comes from the observation of longitudinal streaks for the case of sediment-laden flows, including those over rough beds (Grass 1971). Sumer & Deigaard (1981), Yung, Merry & Bott (1989), Rashidi, Hetsroni & Banerjee (1990), Garcia, Nino & Lopez (1995) and Nino & Garcia (1996) provided convincing experimental evidence of the influence of bursts on the incipient movement of solid particles. Pressure fluctuations caused by turbulent eddies could provide a physical explanation of the connection between particle entrainment and coherent structures. This conjecture is supported by Schewe (1983), Hofland (2005) and Detert, Nikora & Jirka (2010b), among others. For example, extensive evidence of the links between the bursting phenomenon and drag and lift fluctuations on the bed were given by Garcia *et al.* (1996), who showed that ejection events downstream of shear layers are primarily responsible for lifting fine particles from the bed. In turn, Hofland *et al.* (2005), who worked with bedload particles, showed that the peak drag force correlated with positive longitudinal-velocity fluctuations and negative vertical-velocity fluctuations (sweep events). These examples support the conjecture that the lift and drag fluctuations are correlated with turbulent ejections and sweeps, respectively. However, to reveal the exact mechanisms of this correlation, the simultaneous consideration of pressure fluctuations and the associated velocity field is required.

Our data for both the drag and lift components exhibit regions of high-amplitude pressure fluctuations occurring at irregular time intervals. Figure 13 shows the time series of drag fluctuations $p'_D$ (from sensor 9 as an example), normalised by the standard deviation, for $S_b = 0.003$ and $H/D = 7.5$. The entire time series in figure 13(a) shows the presence of high-amplitude positive and negative peaks at various times. The maximum positive and maximum negative pressure peaks were determined from figure 13(a) and these are shown in figure 13(b,c), respectively. The maximum positive pressure peak reaches a value of $p'_D/\sigma_D = +10.1$, whereas the maximum negative pressure peak reaches a value of $p'_D/\sigma_D = -9.81$. These values indicate that the positive peaks of the drag fluctuations are only slightly more extreme than the negative peaks, in agreement with figures 11(d) and 12(c). The time series of lift fluctuations $p'_L$ (from sensor 15 as an example), normalised by its standard deviation, for $S_b = 0.003$ and $H/D = 7.5$ is shown in figure 14. As for the drag fluctuations, the times-series plots of the lift fluctuations in figure 14(a) also show the presence of high-amplitude positive and negative peaks at irregular time intervals. However, figure 14(b,c) shows that the maximum positive pressure peak reaches a value of $p'_L/\sigma_L = +6.0$, whereas the maximum negative pressure peak is more extreme, around $p'_L/\sigma_L = -11.4$. This indicates that the positive peaks of the lift fluctuations are less extreme than the negative peaks, i.e. the signal is negatively skewed, as indicated by the negative values of $\sigma_L$ in figures 11 and 12. Regions of high-amplitude pressure fluctuations for $S_b = 0.003$ and $H/D = 7.5$ were also studied using the signals from other sensors (for both drag and lift). The results show that the maximum positive and negative pressure peaks of drag fluctuations vary between $p'_D/\sigma_D = +7.13$ and $+10.1$ and $p'_D/\sigma_D = -7.05$ and $-9.81$, respectively. For the lift fluctuations, the maximum positive and negative pressure peaks vary between $p'_L/\sigma_L = +3.93$ and $+8.59$ and $p'_L/\sigma_L = -7.58$ and $-11.41$, respectively. These results qualitatively agree well with the values reported by Schewe (1983). The maximum positive and negative pressure peaks when normalised by $\tau_0$ give $p'_D/\tau_0 = +26.22$ and $p'_D/\tau_0 = -25.48$, respectively. Interestingly, Detert *et al.* (2010a) obtained a much higher value of the maximum positive pressure peak of $p'_D/\tau_0 = +40$, which could be explained by higher protrusion
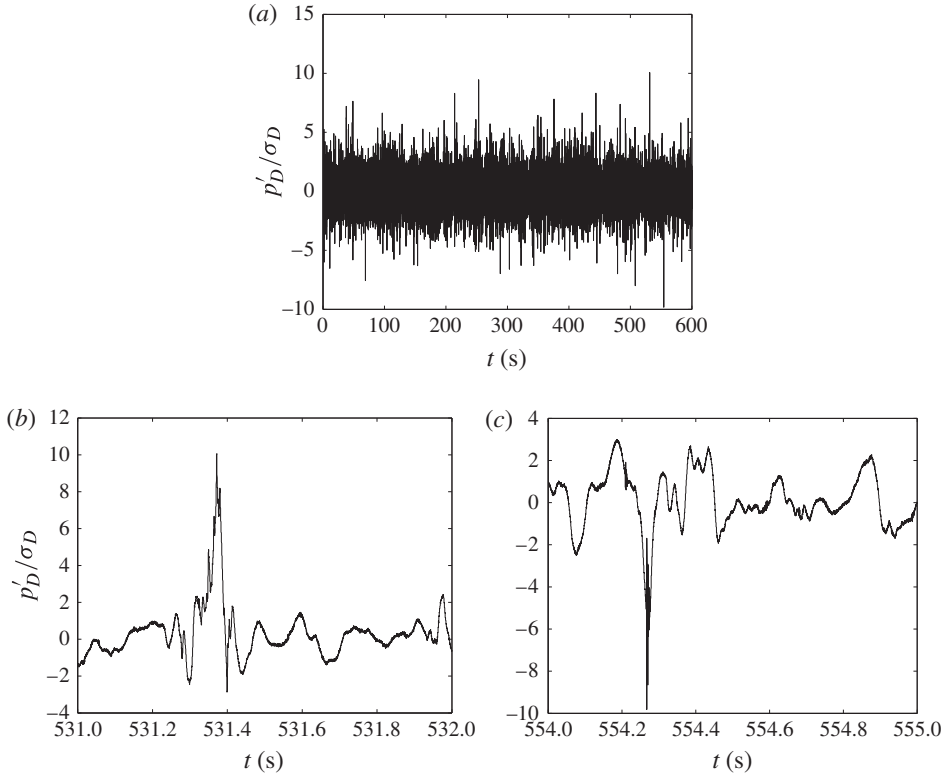
FIGURE 13. Time series of normalised drag fluctuations (*a*) for the entire measurement duration of 10 min, and highlighting (*b*) the maximum positive pressure peak and (*c*) the maximum negative pressure peak for $S_b = 0.003$ and $H/D = 7.5$. Sensor 9 is used as an example.

of their drag sensor into the flow as well as because they measured the differential pressure with reference to atmospheric pressure.

Figure 12(*a,b*) suggests that the standard deviations of drag and lift forces are linearly dependent on the bed slope and relative submergence. This observation is in agreement with a linear dependence of $\sigma$ with the bed shear stress. Indeed, the linear relation between $\sigma$ (for drag or lift) and $\tau_0$ can be presented as

$$\sigma_{D,L} = k_{D,L}\tau_0 = k_{D,L}\rho_f u_*^2 = k_{D,L}\rho_f gHS_b = k_{D,L}\rho_f gDS_b\frac{H}{D}, \tag{5.4}$$

where $k_D$ and $k_L$ are drag and lift coefficients, respectively. Equation (5.4) shows that $\sigma$ is linearly dependent on both bed slope and submergence. It is important to note that the bulk estimate for shear velocity is used in (5.4), whereas, for data interpretation, shear velocity was estimated from the shear stress profile. Coefficients $k_D$ and $k_L$, evaluated using the spatially averaged values of $\sigma_D$ and $\sigma_L$, are shown in figure 15 as functions of $H/D$. It can be seen that $k_D$ increases fairly linearly with $H/D$. For $k_L$, a sharp increase is observed when $H/D$ increases from 2.5 to 5.0. Further increase in $H/D$ has no effect on the value of $k_L$. Given that the flow Reynolds number is also increasing as $H/D$ is increasing, it is not possible to isolate the specific dependence of $k_L$ and $k_D$ on either $Re_p$ or $H/D$.
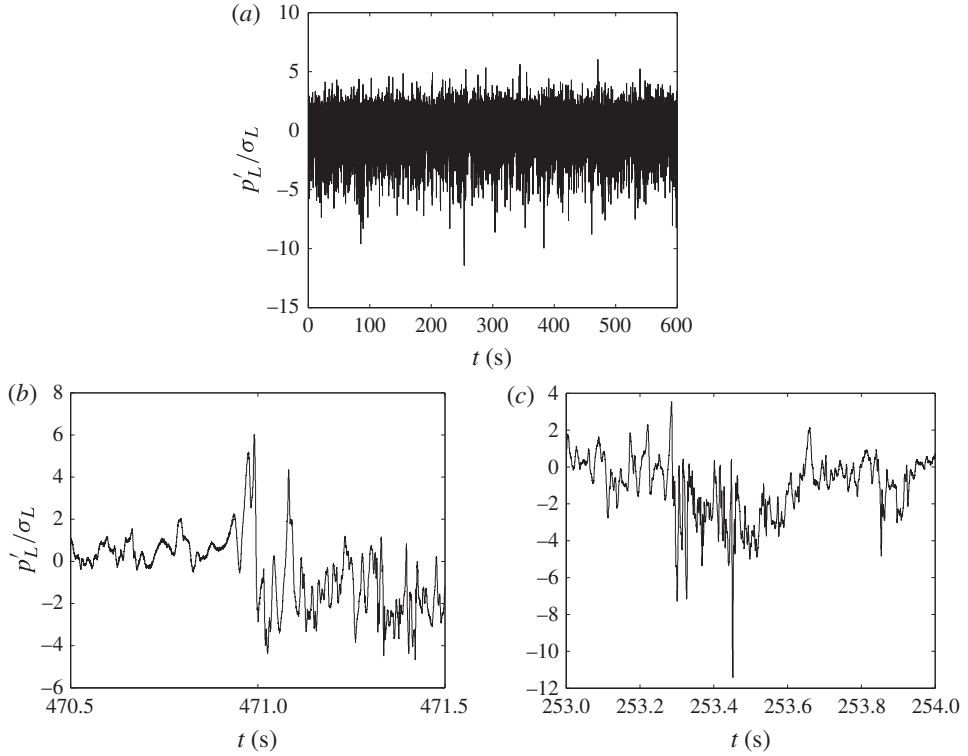
FIGURE 14. Time series of normalised lift fluctuations (*a*) for the entire measurement duration of 10 min, and highlighting (*b*) the maximum positive pressure peak and (*c*) the maximum negative pressure peak for $S_b = 0.003$ and $H/D = 7.5$. Sensor 9 is used as an example.
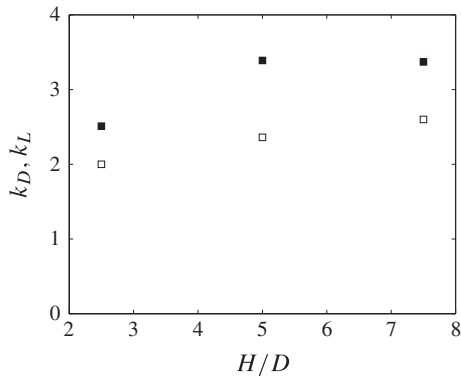


FIGURE 15. Coefficients $k_D$ (□) and $k_L$ (■) as a function of $H/D$.

As discussed in §1, a link between the standard deviation of wall pressure fluctuations and the mean bed shear stress was empirically studied for flows over smooth and rough impermeable walls. These studies show that $\sigma_p = (2.19–3.8)\tau_0$ (Willmarth & Wooldridge 1962; Willmarth & Roos 1965; Farabee & Casarella 1991).

Hinze (1975) also highlighted that the proportionality coefficient changes with the flow Reynolds number and suggested that an average value of 3 can be used, i.e. $\sigma \approx 3\tau_0$. The $\sigma \approx \tau_0$ dependence was mainly demonstrated for impermeable (continuous) smooth and rough beds. More recently, Detert *et al.* (2004) reported similar results with $\sigma \approx (3\text{–}3.5)\tau_0$ for hydraulically rough flow over a multi-layered and homogeneous stratum of spherical particles of diameter 10 mm. Smart & Habersack (2007) showed that this dependence is also observed in gravel-bed rivers, and through their field data reported that $\sigma \approx 3\tau_0$. In the present study, the values for $k_D$ and $k_L$ (figure 15) vary from 2.0 to 2.6 and from 2.5 to 3.4, respectively, and thus agree well not only with the data for smooth and continuous rough beds but also with the data for discontinuous rough granular beds. Furthermore, the Reynolds-number dependence of $k_D$ and $k_L$ in the current study is also possible for flows over granular beds in open-channel flows, although its exact effect is impossible to separate, using our dataset, from the flow submergence effect.

## 5.2. *Correlations, convection velocity and characteristic scales*

### 5.2.1. *Spatial and temporal correlations*

The data allowed the estimation of one-dimensional and two-dimensional sections of the three-dimensional correlation functions for drag forces, $R_{DD}(\Delta x, \Delta y, \tau)$, lift forces, $R_{LL}(\Delta x, \Delta y, \tau)$, and drag–lift combinations, $R_{DL}(\Delta x, \Delta y, \tau)$. The two-dimensional section of correlation function $R_{ij}(\Delta x, \Delta y = 0, \tau)$ refers to two sensors separated by a distance $\Delta x$ in the longitudinal direction, with $\tau$ being the time delay. Similarly, the correlation $R_{ij}(\Delta x = 0, \Delta y, \tau)$ refers to sensors separated by a distance $\Delta y$ in the transverse direction. The one-dimensional sections $R_{ij}(\Delta x = 0, \Delta y = 0, \tau)$ represent temporal autocorrelation functions. In the following plots, the time delay has been normalised with outer flow units, i.e. $\tau U_b/H$.

Figure 16(a) shows the correlation functions $R_{DD}(\Delta x = 27.7\ \text{mm}, \Delta y = 0, \tau)$ of drag fluctuations for two particles (8 and 9 in figure 3) for $H/D = 7.5$, 5.0 and 2.5 at $S_b = 0.003$. At $\tau U_b/H = 0$, the correlation of drag fluctuations is small. However, a strong correlation occurs at a finite temporal separation. The correlation reaches a maximum value of 0.38 at $H/D = 7.5$ and 5.0, which reduces marginally to a value of 0.34 at $H/D = 2.5$. The separation time at which the maximum correlation is achieved increases as $H/D$ is reduced. This is indicated by a shift in the maximum correlation peak in figure 16(a) and reflects the fact that the flow, and consequently the convection velocity of the pressure signal, is getting slower, which will be further discussed in the following section.

The correlations $R_{DD}(\Delta x = 0, \Delta y = 32\ \text{mm}, \tau)$ of drag fluctuations between particles 3 and 4 in the transverse direction (figure 3) are shown in figure 16(b). The correlations are weak compared to those seen in figure 16(a), probably because the turbulent eddies are elongated in the longitudinal direction more than in the transverse direction. It can also be seen that the separation time, at which the maximum correlation occurs, is approximately zero and does not change with $H/D$, indicating that the transverse component of the velocity is close to zero at all submergences.

The correlations $R_{LL}(\Delta x = 27.7\ \text{mm}, \Delta y = 0, \tau)$ of lift fluctuations between particles 16 and 14 in the longitudinal direction (figure 3) are shown in figure 16(c). Although both the drag–drag and lift–lift sensors are separated by the same longitudinal separation, slightly weaker correlations are seen for the lift fluctuations. The maximum correlation value of 0.29 is observed at $H/D = 7.5$, which reduces significantly to
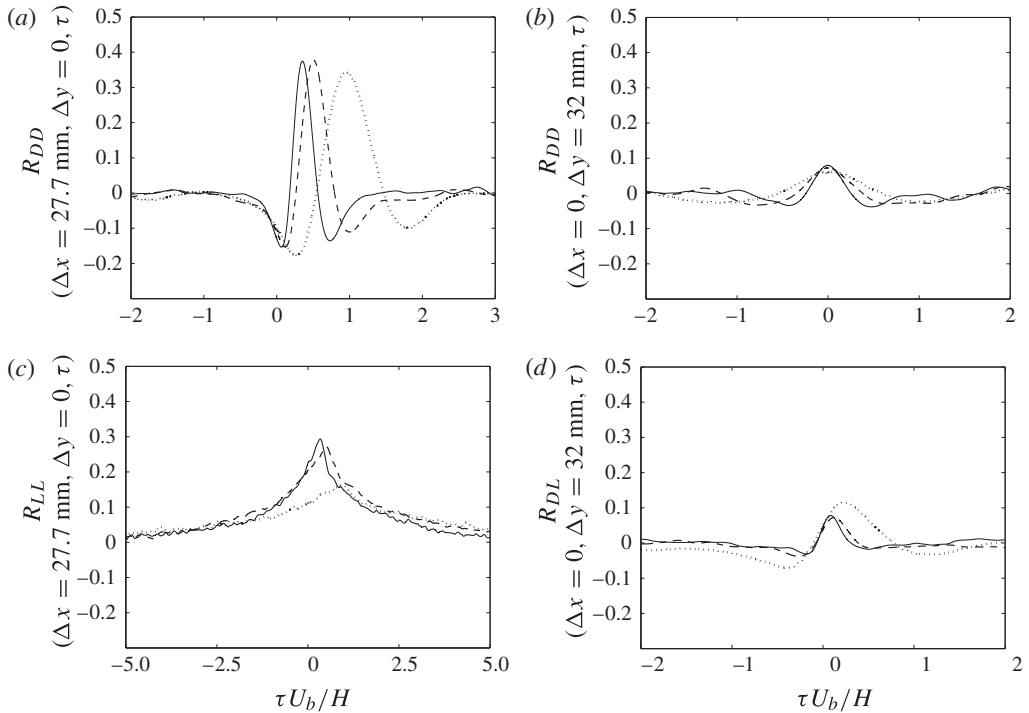
FIGURE 16. Correlation functions of (*a,b*) drag fluctuations for (*a*) longitudinal and (*b*) transverse separation, (*c*) lift fluctuations for longitudinal separation and (*d*) drag–lift fluctuations for transverse separation at $S_b = 0.003$. Lines: solid, $H/D = 7.5$; dashed, $H/D = 5.0$; dotted, $H/D = 2.5$.

0.16 at $H/D = 2.5$. It is also interesting to observe that, unlike in figure 16(*a*), where a local minimum for cross-correlation is followed by a local maximum for drag fluctuations, the lift fluctuations in figure 16(*c*) do not show such behaviour. Instead, only a single peak that corresponds to the maximum correlation is seen for all three submergences.

To find out whether drag and lift fluctuations are correlated in time, correlations $R_{DL}(\Delta x = 0, \Delta y = 16\ \text{mm}, \tau)$ of drag and lift fluctuations (particles 5 and 16 in figure 3) are shown in figure 16(*d*). It can be seen that, at $\tau U_b/H = 0$, the drag and lift fluctuations are weakly correlated, and only a moderate correlation occurs at a finite temporal separation for $H/D = 7.5$ and 5.0 and a slightly stronger correlation of 0.115 is seen for $H/D = 2.5$. These correlations of drag and lift fluctuations are of the same magnitude as seen in figure 16(*b*) for drag–drag fluctuations in the transverse direction and are relatively lower than those seen in figure 16(*a*) for drag–drag fluctuations in the longitudinal direction. A positive correlation at $\tau U_b/H = 0$ indicates that, on average, drag and lift have the same sign at the same moment. This is probably due to a mechanism in which the streamwise velocity creates drag forces (stagnation pressure) and lift forces (streamline contraction) simultaneously. Other investigators (Hofland 2005; Dwivedi 2010; Chan-Braun, Villalba & Uhlmann 2013) have reported values of maximum correlation of drag and lift fluctuations between 0.26 and 0.55. The higher correlation values could be partly explained by the fact that they relate to a single particle rather than to two adjacent particles, as in our case. The correlation

level depends, in general, on the Reynolds number, particle shape and $H/D$ ratio. While Dwivedi (2010) directly measured lift and drag on the same spherical particle, Hofland (2005) measured the forces indirectly by the difference of two simultaneous pressure measurements. He measured both the drag and lift fluctuations on a single particle that was cubical in shape, whereas, in the present study, each individual particle is either measuring lift or drag fluctuations and the minimum separation between the two is 16 mm. The reduced value of maximum correlation is therefore directly influenced by the separation between two pressure sensors. It should also be mentioned that Hofland (2005) and Dwivedi (2010) have reported measurements of the differential pressure with reference to atmospheric pressure. Apart from the differences in the maximum correlation value, it is promising to see that the cross-correlation in the present study resembles the typical shape, with a local minimum for a negative separation in time and a maximum for a positive separation in time, as also reported by Hofland (2005), Dwivedi (2010) and Chan-Braun *et al.* (2013).

Correlation between other drag–drag, lift–drag and lift–drag sensors for the same flow configurations as above also showed similar trends to those seen in figure 16 (not shown here).

Temporal autocorrelations $R_{DD}(\Delta x = 0,\ \Delta y = 0,\ \tau)$ and $R_{LL}(\Delta x = 0,\ \Delta y = 0,\ \tau)$ were evaluated for both drag and lift fluctuations, respectively. Figure 17(*a*) shows examples of the autocorrelation functions of the drag and lift fluctuations at $S_b = 0.003$ and $H/D = 7.5$. For the drag and lift fluctuations, the sensors placed in positions 1 and 14 (figure 3), respectively, were used. It can be seen that the drag fluctuations exhibit a pronounced local minima of $-0.19$, whereas for the lift fluctuations, no local minimum exists. Figure 17(*a*) also shows that the autocorrelations of the drag fluctuations vanish to zero much more rapidly compared to that for the lift fluctuations. These results indicate that the lift fluctuations are correlated over much longer time durations. Furthermore, previous studies have shown that the autocorrelation of wall pressure fluctuations at smooth and rough surfaces under turbulent boundary layers exhibit local minima (Burton 1973; Kim 1989; Quadrio & Luchini 2003), similar to those observed in the present case for the drag fluctuations. More recently, Chan-Braun (2012) observed a local minimum in the autocorrelation function of the total drag force acting on a particle. It was conjectured that the minimum peak might be linked to the effect of pressure on the force on a particle. The present results lend support to this conjecture.

For the same flow configuration, the autocorrelations of drag fluctuations from all other drag sensors (see figure 3) collapsed very well, as one would expect for homogeneous uniform flow. To preserve clarity, figure 17(*b*) shows only autocorrelations from drag sensors placed upstream of position 1 in figure 3. An excellent collapse is seen up to the first zero crossing, with only marginal variations in the local minimum values. A satisfactory collapse is likewise observed in the autocorrelations of the lift fluctuations shown in figure 17(*c*) but only when $\tau U_b/H > 4$. The absence of a local minimum for the lift fluctuations is also evident for all sensors shown in figure 17(*c*). Similar trends to those seen in figure 17 were also observed for all other flows (not shown here).

The autocorrelations of both the drag and lift fluctuations were then spatially averaged in the longitudinal direction and the effects of submergence at a fixed bed slope were studied. The averaged autocorrelation functions are shown in figure 18 for the bed slope of 0.003. Effects of $H/D$ are clearly evident in figure 18(*a*) for the drag fluctuations. As $H/D$ is reduced, it takes longer for the autocorrelation to reach a local minimum. The minimum correlation value also decreases with decreasing $H/D$ (from $-0.175$ at $H/D = 7.5$ to $-0.195$ at $H/D = 2.5$).
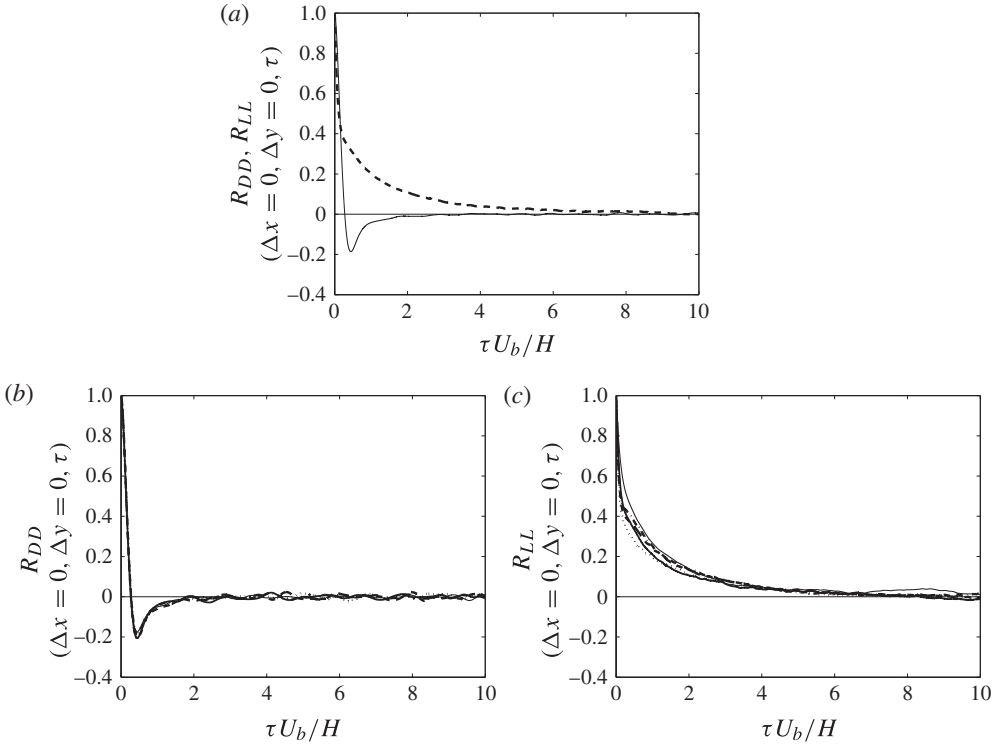
FIGURE 17. Temporal (*a*) autocorrelation of drag (solid line) and lift (dashed line) fluctuations for sensors placed in positions 1 and 14, respectively; (*b*) autocorrelation of drag fluctuations for sensors placed in positions 9 (solid), 8 (dotted), 7 (dashed), 6 (dashed-dotted) and 5 (thick solid); and (*c*) autocorrelation of lift fluctuations for sensors placed in positions 17 (solid), 16 (dotted), 14 (dashed), 18 (dashed-dotted) and 19 (thick solid) at $S_b = 0.003$ and $H/D = 7.5$.
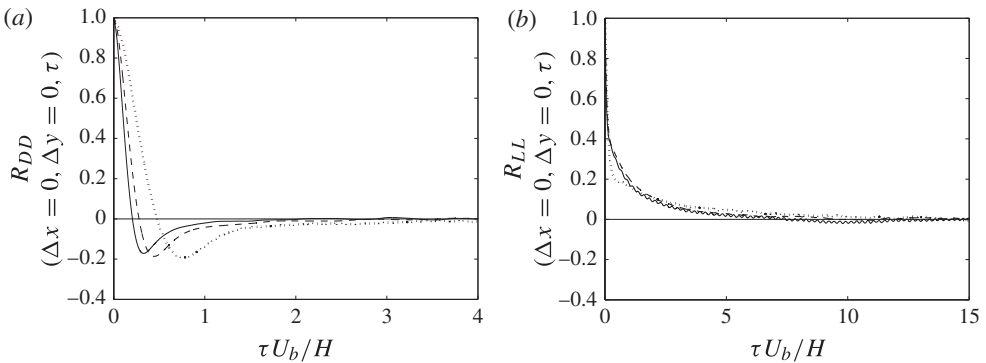


FIGURE 18. Spatially averaged autocorrelation of the (*a*) drag fluctuations and (*b*) lift fluctuations at $S_b = 0.003$: $H/D = 7.5$ (solid); $H/D = 5.0$ (dashed); $H/D = 2.5$ (dotted).

Figure 18(*b*) shows that, for the lift fluctuations, the autocorrelation at $H/D = 7.5$ almost overlaps with $H/D = 5.0$. However, at $H/D = 2.5$, the autocorrelation decays much more rapidly for small separation times. At $\tau U_b/H > 1$, the autocorrelation then overlaps with the other two curves for the higher submergences.
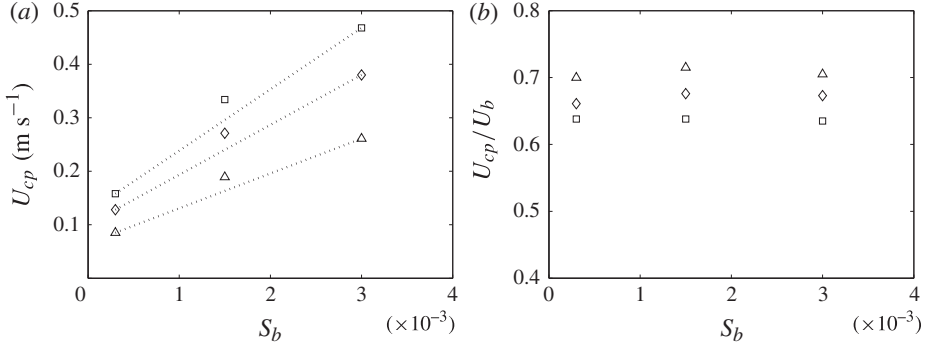
FIGURE 19. Spatially averaged (*a*) convection velocities (obtained from pressure data) and (*b*) normalised (by bulk velocities) as a function of bed slope. Symbols: $\square$, $H/D = 7.5$; $\diamond$, $H/D = 5.0$; $\triangle$, $H/D = 2.5$. Dotted lines are linear fits through the data points in panel (*a*).

Chan-Braun *et al.* (2013) reported that, for their larger spherical particles ($Re_p = 235$), the curves of both drag and lift fluctuations exhibited local minima of negative values of $-0.25$ and $-0.18$, respectively. However, for their smaller spherical particles ($Re_p = 188$), a local minimum only existed for the drag fluctuations while it was absent for the lift fluctuations. Although there is a dramatic difference in $Re_p$, which is in the range of 538–918 in the present case (figure 18), the existence of a local minimum for drag fluctuations agrees well with their observations. However, the present results do not show a local minimum for the lift fluctuations. The value of $Re_p$ does not seem to affect this characteristic, contrary to the observations in the study of Chan-Braun *et al.* (2013).

### 5.2.2. *Convection velocities*

The eddies in turbulent boundary layers and open-channel flows propagate downstream at a speed that is usually assumed to be close to the local time-averaged flow velocity, and which is referred to as the eddy convection velocity (Townsend 1976; Nikora & Goring 2000; Cameron & Nikora 2008). It has been shown that this assumption is reasonably valid for open-channel flows, with the exception of a near-bed flow region ($\sim 0.1H$ thick) where the eddy convection velocity exceeds the local time-averaged velocities (Nikora & Goring 2000; Cameron & Nikora 2008).

In the present study, we compare eddy convection velocity with the convection velocities for the pressure fluctuations obtained from the drag sensors positioned in the longitudinal direction (figure 3). The computation of the pressure convection velocity, $U_{cp}$ (subscript $p$ refers to pressure), requires a time delay $\tau_{max}$ between two pressure sensors separated by a distance $\Delta x$ that corresponds to the maximum correlation. The convection velocity $U_{cp}$ can then be calculated as $\Delta x / \tau_{max}$. Thus, $U_{cp}$ was obtained using cross-correlation functions $R_{DD}(\Delta x, \Delta y = 0, \tau)$ for drag sensors 9 and 8, 8 and 7, and so on (figure 3). A spatially averaged value was then calculated by averaging values of $U_{cp}$ in the longitudinal direction.

Figure 19(*a*) shows $U_{cp}$ as a function of bed slope for all three submergences. It can be seen that $U_{cp}$ increases approximately linearly with $S_b$ at each $H/D$. Also, the rate of increase in $U_{cp}$ with $S_b$ increases with increasing $H/D$. The convection velocity of the dominant eddies is shown to be close to the bulk flow velocity and, therefore, as $H/D$ increases, an increment in the mean flow velocity results in an
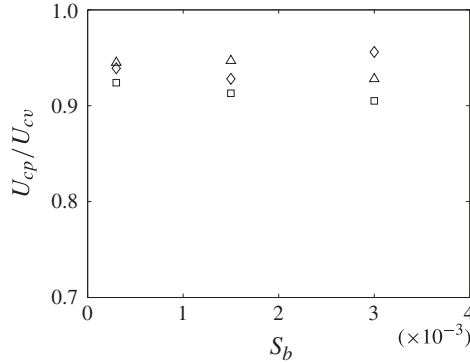
FIGURE 20. Ratio $U_{cp}/U_{cv}$ as a function of bed slope: $\square$, $H/D = 7.5$; $\lozenge$, $H/D = 5.0$; $\triangle$, $H/D = 2.5$.

increased eddy convection velocity. If we assume that the bed pressure heterogeneities are footprints of these large eddies, then we may expect that the pressure convection velocity should also grow with $H/D$, as seen in figure 19(*a*). When the pressure convection velocities are normalised by their respective bulk velocities, the ratio $U_{cp}/U_b$ seems to be unaffected by the bed slope (figure 19*b*). At any fixed bed slope, however, there is a consistent tendency for the ratio $U_{cp}/U_b$ to reduce with an increase in $H/D$ (and Reynolds number). Figure 19(*b*) shows that values of $U_{cp}/U_b$ are in the range of 0.64–0.72. The obtained $U_{cp}/U_b$ values are therefore within the range 0.56–0.83 reported for boundary layers over impermeable walls by Willmarth & Wooldridge (1962). The present results also agree well with Chan-Braun *et al.* (2013), who reported values for $U_c/U_b$ between 0.58 and 0.71 (their convection velocity relates to direct estimates of the fluctuating drag and lift forces). The ratio $H/D$ for one of their flow cases was 5.56 and thus comparable with the present results. However, their simulations were carried out at much smaller bulk Reynolds number ($Re_b = 2870$–2880), friction Reynolds number ($Re_* = 188$–233) and particle Reynolds number ($Re_p = 14$–46), whereas the present study expands the range of $Re_b$ up to a value of 88 729, $Re_*$ up to a value of 6911 and $Re_p$ up to a value of 918.

Eddy convection velocities from PIV mode 2 were evaluated using space–time correlation functions $R_{uu}(\Delta x, \Delta \tau, z)$ of streamwise velocity fluctuations following the procedure outlined in Cameron & Nikora (2008). The convection velocities estimated from the PIV data will be denoted as $U_{cv}$ (subscript $v$ refers to velocity). For all flow configurations, $U_{cv}$ was evaluated at a distance of 1.5 mm above the roughness tops. This is the minimum vertical distance above the roughness tops for which the convection velocities could be evaluated for all flow configurations. Similar trends to those seen for $U_{cp}$ in figure 19(*a*) were also observed for $U_{cv}$ (not shown here). At each flow configuration, $U_{cv}$ is slightly higher than $U_{cp}$, as one would expect due to the difference in vertical measurement positions for velocity and pressure, and this is represented in figure 20. The close agreement between the estimates of convection velocity, $U_{cp}/U_{cv} \sim 0.9$–0.95, lends further weight to the argument that measured space–time pressure heterogeneities represent the footprint of large eddies.

### 5.2.3. *Characteristic time scales*

The integral time scales for both the drag and lift fluctuations were calculated using temporal autocorrelation functions. The integration domain for the determination of
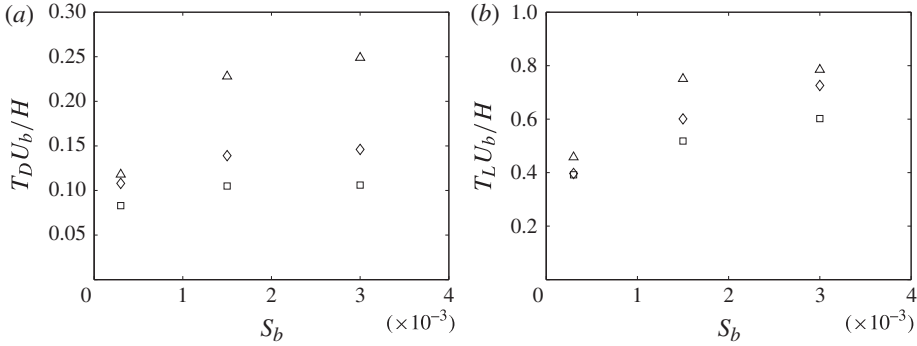
FIGURE 21. Integral time scale (integrated up to first zero crossing) of (*a*) drag and (*b*) lift fluctuations as a function of bed slope: $\square$, $H/D = 7.5$; $\lozenge$, $H/D = 5.0$; $\triangle$, $H/D = 2.5$.

the integral scales can be specified in a number of ways (e.g. Tritton 1988; Katul & Parlange 1995). In the present study, we integrate up to the first zero crossing of the temporal autocorrelations shown in figure 17. The obtained time scales were normalised with outer flow units, i.e. $T_{D,L}U_b/H$, where $T_D$ and $T_L$ are the integral time scales of drag and lift, respectively. The integral time scales of drag and lift fluctuations as a function of bed slope are plotted in figure 21 for all submergences. Figure 21(*a*) shows that, for fixed $S_b$, normalised time scales of drag fluctuations increase with decreasing $H/D$, suggesting that the relative size (in terms of flow depth) of the dominant pressure disturbances increases with decrease in flow submergence. This effect becomes more pronounced as $S_b$ increases. However, the dependence of the time scales of drag fluctuations on bed slope for fixed $H/D$ is limited up to an intermediate value of $S_b = 0.0015$ only. Further increase in $S_b$ does not affect the time scales for $H/D = 5.0$ and 7.5. For the lowest value of $H/D = 2.5$, the time scales of drag fluctuations continue to increase with increasing bed slope. The normalised time scales for lift fluctuations in figure 21(*b*) also show an increase with decreasing $H/D$ for fixed $S_b$. However, the time scales of lift are approximately 3–6 times larger than those of drag fluctuations depending on both slope and $H/D$, as observed previously in figure 17. Chan-Braun *et al.* (2013) reported values of time scales (scaled in outer flow units) of 0.14 and 0.10 for drag and lift, respectively, with their $H/D = 5.0$ and $Re_p = 235$. In the present study, at $H/D = 5.0$ and $Re_p$ varying between 170 and 918, the normalised time scale of drag fluctuations varies between 0.11 and 0.15 (for various bed slopes), which is in agreement with the data of Chan-Braun *et al.* (2013). However, the time scale of lift at $H/D = 5.0$ varies between 0.40 and 0.73 compared to their value of only 0.10.

### 5.2.4. *Spatial scales of pressure fluctuations*

Using the three-dimensional correlation function $R_{DD}(\Delta x, \Delta y, \tau)$, the characteristic spatial scales can be evaluated. Two types of spatial scales are presented here. First is a spatial scale typical of a structure at fixed time (its length as deduced, for example, from a snapshot of the pressure field) and second a spatial scale corresponding to the distance travelled by the structure during its lifetime. It is important to note that the correlation of only the drag fluctuations was considered in determining the spatial scales, as the present layout of the pressure sensors (figure 3) does not permit a similar analysis for the lift sensors. Also, because of the relatively low correlation values
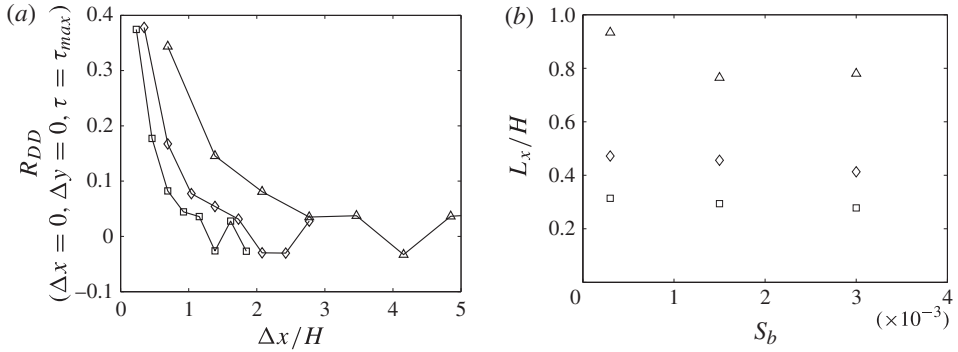
FIGURE 22. (a) The correlation functions $R_{DD}(\Delta x, \Delta y = 0, \tau = \tau_{max})$ of drag fluctuations at $S_b = 0.003$ and (b) the integral spatial lifetime scales for longitudinal separations. Symbols: $\square$, $H/D = 7.5$; $\diamond$, $H/D = 5.0$; $\triangle$, $H/D = 2.5$.

between sensors located in the transverse direction (as seen in figure 16$b$), it was not possible to determine spatial scales in the transverse direction. We now describe the method used to evaluate the spatial lifetime scales.

The spatial lifetime scale in the longitudinal direction is determined from the correlation function $R_{DD}(\Delta x, \Delta y = 0, \tau = \tau_{max})$. The condition $\tau = \tau_{max}$ refers to the time delay when the correlation reaches a maximum. As the longitudinal separation between the pressure sensors increases, the maximum correlation value reduces and the spatial separation, at which the coefficient reaches zero, can be used as the characteristic spatial lifetime scale of the pressure pattern.

Figure 22($a$) shows the correlation of drag fluctuations for longitudinal separations (normalised by $H$) at $S_b = 0.003$ for all three submergences. At $H/D = 2.5$, an extended region of significantly higher correlation is seen in figure 22($a$) compared to those at higher $H/D$ of 7.5 and 5.0. The correlation vanishes to zero after longitudinal separations of $1.27H$ and $1.90H$ at $H/D = 7.5$ and 5.0, respectively, whereas, at $H/D = 2.5$, the longitudinal separation is much larger, reaching $3.8H$. The correlations of drag fluctuations for the other two bed slopes were also evaluated (not shown here) and similar trends to those seen in figure 16($a$) were observed.

The integral spatial lifetime scales for longitudinal separations were then calculated using $R_{DD}(\Delta x, \Delta y = 0, \tau = \tau_{max})$. Similar to §5.2.3, we integrate up to the first zero crossing of the correlations as shown in figure 22($a$). Figure 22($b$) presents the longitudinal integral lifetime scales (normalised by $H$) as a function of bed slope for all three submergences. It can be seen that the longitudinal spatial lifetime scale, $L_x/H$, is clearly dependent on $H/D$. As submergence increases at fixed bed slope, the structures cover smaller spatial areas in terms of flow depths. Figure 22($b$) also shows that, for $H/D = 5.0$ and 7.5, $L_x/H$ decreases with increasing bed slope. However, for $H/D = 2.5$, a decrease in $L_x/H$ is observed up to an intermediate value of $S_b = 0.0015$ only. Further increase in $S_b$ has no effect on $L_x/H$. The results therefore reveal that the spatial lifetime scales show greater dependence with bed slope for higher submergences only.

Next we describe the method to evaluate the second type of spatial scale, i.e. the length scale of the structure itself. The length scale in the longitudinal direction is determined by the correlation function $R_{DD}(\Delta x, \Delta y = 0, \tau = 0)$. As the longitudinal separation between the pressure sensors increases, the correlation coefficient value at
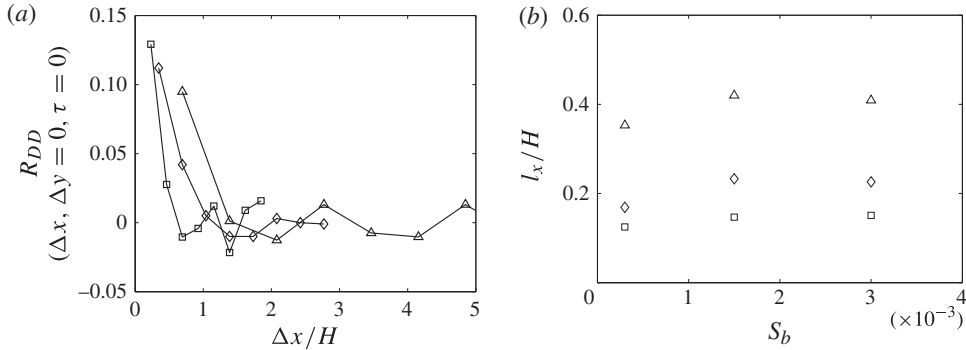
FIGURE 23. (*a*) The correlation functions $R_{DD}(\Delta x, \Delta y = 0, \tau = 0)$ of drag fluctuations at $S_b = 0.003$ and (*b*) the integral length scales for longitudinal separations. Symbols: $\square$, $H/D = 7.5$; $\lozenge$, $H/D = 5.0$; $\triangle$, $H/D = 2.5$.

zero time delay reduces and the spatial separation at which the coefficient reaches a value of zero can be used as the characteristic length scale of the pressure pattern.

Figure 23(*a*) shows the correlation of drag fluctuations for longitudinal separations (normalised by the flow depth) at $S_b = 0.003$ for all three submergences. Similar trends to those seen in figure 22(*a*) are also evident in figure 23(*a*). It can be seen in figure 23(*a*) that correlations vanish to zero after longitudinal separations of $0.55H$, $1.1H$ and $1.4H$ at $H/D = 7.5$, 5.0 and 2.5, respectively. These results indicate that the length scales of the structure itself are much smaller than the lifetime scales, as one would expect.

The integral length scales $l_x$ were computed by integrating the correlations (as shown in figure 23*a*) up to the first zero crossing. Figure 23(*b*) shows the integral length scales (normalised by $H$) as a function of bed slope for all three submergences. It can be seen that the normalised integral length scales $l_x/H$ are dependent on submergence at fixed bed slope. With decreasing $H/D$, the integral length scales cover larger spatial distances in terms of flow depths. These trends are similar to those seen in figure 22(*b*) for the lifetime scales. If it is assumed that the spatial extent of the correlation in the pressure field is a direct reflection of the spatial correlation in the overlying velocity field, then it appears that velocity and consequently pressure structures are spreading out more as submergence decreases, possibly because the largest velocity structures are being vertically confined by the free surface. It is also interesting to see in figure 23(*b*) that, at fixed submergence, the bed slope has very little or no effect on $l_x/H$ as $S_b$ is reduced from 0.003 to 0.0015. However, further reduction in $S_b$ to a value of 0.0003 has a relatively significant effect on $l_x/H$. These results indicate that the integral length scales show dependence on both submergence and bed slope, which is the case for the integral spatial lifetime scales as well. The changes due to bed slope are, however, very small for both types of length scales.

### 5.3. *Spectra*

The spectra of the pressure signals were investigated to explore the spectral content of drag and lift fluctuations and also to address the question as to what extent noise influences the pressure statistics. The spectra were estimated by the averaged modified periodogram method of Welch (1967). Segment lengths of $n = 2^{12}$ with 50 % overlap were used and each segment was weighted with a Hamming window of the same length.
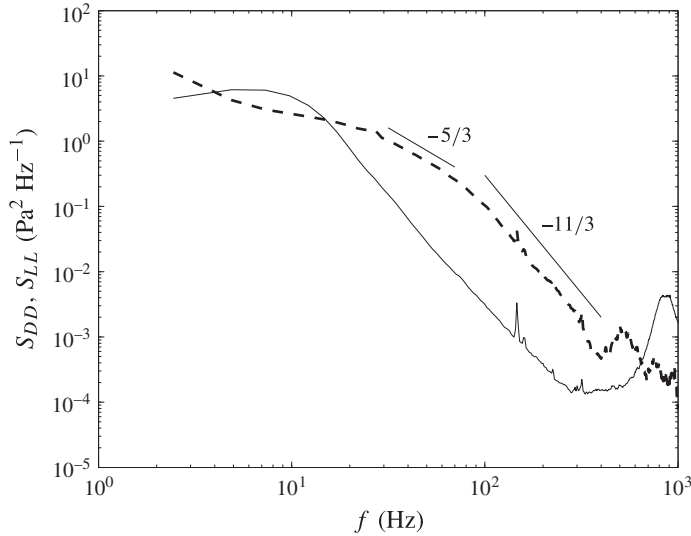
FIGURE 24. Spatially averaged spectra of drag (solid line) and lift (dashed line) fluctuations for $H/D = 7.5$ and $S_b = 0.003$.

Frequency spectra of drag and lift fluctuations were computed for all sensors placed in both longitudinal and transverse directions of the flow. A reasonably good collapse of spectral curves for different sensors under the same flow configurations is observed at lower frequencies, with some scatter in the high-frequency range (not shown here). The spectra of all drag and lift sensors placed in the longitudinal direction were then spatially averaged. Figure 24 shows, as an example, the spatially averaged spectra of the drag and lift fluctuations for run 9 ($H/D = 7.5$) at $S_b = 0.003$. The largest spectral contributions to both lift and drag fluctuations are observed at lower frequencies, as could be expected. However, the lift fluctuations show a different behaviour from that of the drag fluctuations in this low-frequency range. The spectra of drag fluctuations show that the spectral magnitude increases gradually in the low-frequency range up to approximately $f = 6.5$ Hz and then starts to decrease over the high-frequency range. The spectral magnitudes of the lift fluctuations, however, decrease over the entire measured frequency range. Both spectra suggest that there are some scaling ranges where spectra decay following some power laws. Figure 24 suggests a $f^{-11/3}$ slope for the drag fluctuations over most of the frequency range. While the lift spectra also display a $f^{-11/3}$ scaling region at high frequency ($f > 90$ Hz), the behaviour differs at low frequency in the range from 20 to 70 Hz, where scaling closer to $f^{-5/3}$ is visible. These results seem to differ from the earlier results of Lee & Sung (2002), Hofland (2005) and Detert *et al.* (2010*a*), who report a $f^{-7/3}$ power law for their turbulent wall pressure spectra, and of Tsuji *et al.* (2007), who found much slower spectral decay, comparable to $f^{-1}$.

At the same time, our study supports the $-11/3$ spectrum of George, Beuther & Arndt (1984), who presented spectral models for turbulent pressure fluctuations in a homogeneous constant mean-shear flow. They showed that the pressure spectrum exhibits $f^{-7/3}$ and $f^{-11/3}$ forms in the inertial subrange for the cases when turbulence–turbulence interaction and turbulence–mean shear contributions dominate, respectively. It is possible that, close to the bed, the turbulence–shear interactions dominate, leading
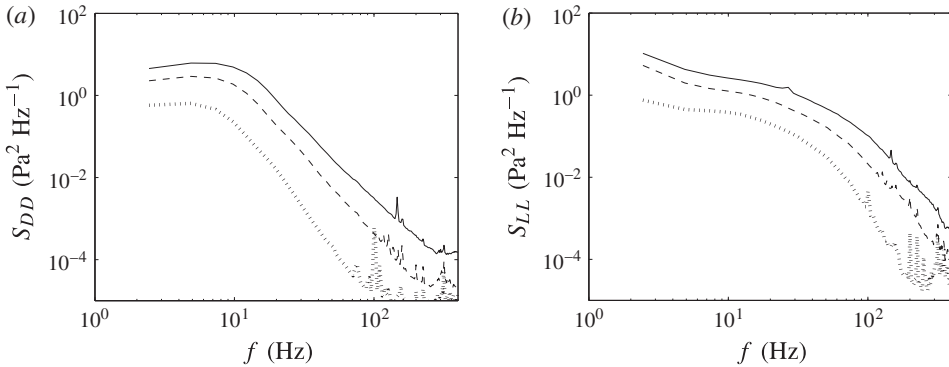
FIGURE 25. Spatially averaged spectra of (*a*) drag and (*b*) lift fluctuations for $S_b = 0.003$. Here $H/D = 7.5$ (solid line); $H/D = 5.0$ (dashed line); $H/D = 2.5$ (dotted line).
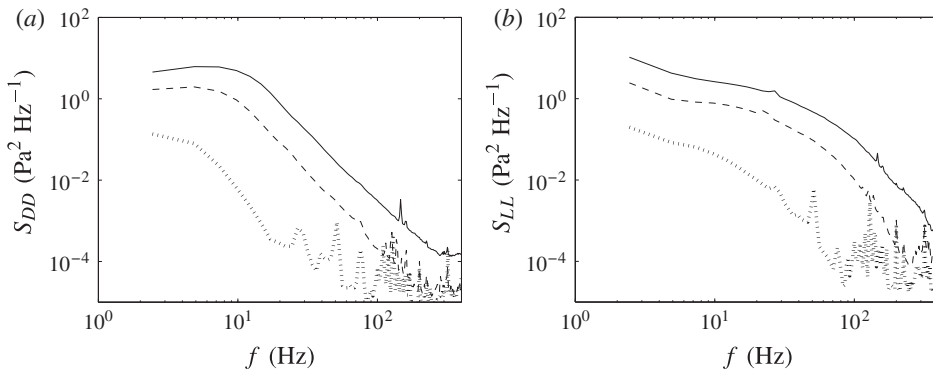


FIGURE 26. Spatially averaged spectra of (*a*) drag and (*b*) lift fluctuations for $H/D = 7.5$. Here $S_b = 0.003$ (solid line); $S_b = 0.0015$ (dashed line); $S_b = 0.0003$ (dotted line).

to a $-11/3$ footprint in the spectra of drag and lift fluctuations. For this issue to be resolved, however, it requires pressure measurements at the bed and in the flow domain.

The effects of $H/D$ on the spectra were then studied at a fixed bed slope. Figure 25 shows the spatially averaged spectra of drag and lift fluctuations at $S_b = 0.003$ for all three submergences. It is evident that the spectral magnitudes of both drag (figure 25*a*) and lift (figure 25*b*) fluctuations increase with $H/D$, in agreement with the behaviour of pressure variances. The slope of the spectra is unaffected at the two higher $H/D$ values, while for $H/D = 2.5$ the spectra of both drag and lift fluctuations show a slightly faster decay in the higher frequency range. Therefore, it can be said that $H/D$ does not seem to influence the shape of the spectra of both lift and drag once it is greater than 5.

The effects of bed slope on the spectra at a fixed submergence were also studied. Figure 26 shows the spatially averaged spectra of drag and lift fluctuations at $H/D = 7.5$ for all three bed slopes. Similar trends to those seen in figure 25(*a*,*b*) are also observed in figure 26(*a*,*b*). At the lowest bed slope of 0.0003, the spectra of both drag and lift fluctuations decay slightly more steeply compared to those at higher bed

slopes. These results indicate that the spectral decay of the drag and lift fluctuations are both dependent on $H/D$ and $S_b$.

Although the recordings were made at a sampling frequency of 10 000 Hz, the high frequencies still produce aliasing noise. Noise levels in the spectra can be seen for most flow cases at $f > 100$ Hz in figures 24–26. However, as $H/D$ and bed slope decrease, the peaks due to the noise start appearing at $f < 100$ Hz, as seen in figure 26(*a*) for $S_b = 0.0003$. This is because, at these slower flows, a low-level pressure signal magnifies the effect of a spurious signal that is always present, for example, electronic noise in this case. Hofland (2005) and Detert *et al.* (2010*a*), who also made use of piezo-resistive pressure sensors, observed similar noise levels in their pressure spectra.

## 6. Summary and conclusions

This work aimed to improve the understanding of pressure forces on non-moving sediment particles in open-channel flows. Measurements were carried out using an array of 23 piezo-resistive differential pressure sensors located within the bed. Simultaneous measurements of the velocity field were made using stereoscopic PIV.

The pressure statistics were investigated by evaluating the standard deviation, skewness and kurtosis of the pressure fluctuations. The results showed that the ratio of standard deviation of pressure fluctuations of lift to drag (i.e. $\sigma_L/\sigma_D$) varies between 1.35 and 1.52. The skewness of the drag fluctuations, $S_D$, is positive while the skewness of the lift fluctuations, $S_L$, is negative. The kurtosis of drag and lift fluctuations, $K_D$ and $K_L$, increase with $H/D$ and $S_b$, reflecting increasing intermittency effects. Regions of positive and negative high-amplitude pressure fluctuations (for both drag and lift) appear in irregular time intervals, which are probably associated with passages and dynamics of large coherent structures. The link between mean shear stress $\tau_0$ and $\sigma$ of the pressure fluctuations, and their dependence on relative submergence (and therefore Reynolds number), was also investigated. It was found that $\sigma_D$ and $\sigma_L$ were 2–2.6 and 2.5–3.4 times $\tau_0$, respectively. While this link between bed shear stress and pressure fluctuations was first derived for smooth beds (Kraichnan 1956), the present results along with those reported by Detert *et al.* (2004) and Smart & Habersack (2007) suggest a technique for estimating local boundary shear stress if instantaneous near-bed pressure measurements can be recorded for flows over rough granular beds. However, the exact flow mechanisms responsible for this link between $\tau_0$ and $\sigma_p$ over rough beds remain to be identified and tested.

The three-dimensional correlation functions for drag–drag, lift–lift and drag–lift pressure fluctuations were evaluated. The drag and lift fluctuations show that these are correlated with a shift in time. Convection velocities of pressure fluctuations, $U_{cp}$, were evaluated by means of two pressure sensors separated by a distance $\Delta x$ in the longitudinal direction. It was found that $U_{cp}$ increases approximately linearly with $S_b$ at all submergences. When $U_{cp}$ is normalised by the bulk velocity, $U_b$, the ratio $U_{cp}/U_b$ showed a dependence on submergence at each bed slope. An increase in $H/D$ and flow Reynolds number causes a reduction in $U_{cp}/U_b$ and this ratio varied between 0.64 and 0.72. Eddy convection velocities, $U_{cv}$, evaluated just above the roughness tops using velocity data from PIV compared well with $U_{cp}$. The integral time scales for both the drag and lift fluctuations were calculated using temporal autocorrelation functions. As the lift fluctuations decayed much more slowly, the integral time scales of lift fluctuations, $T_L$, were found to be approximately 3–6 times greater than those of drag fluctuations, $T_D$. When scaled in outer flow units,

i.e. $T_{D,L}U_b/H$, the normalised integral time scales of both drag and lift fluctuations showed a decrease with increasing submergence at fixed bed slope. The longitudinal spatial lifetime and length scales (i.e. $L_x$ and $l_x$, respectively) were evaluated using three-dimensional correlation functions of drag fluctuations. The integral scales of both types showed a dependence on submergence and bed slope. The results also showed that, as submergence increases, the spatial structures cover smaller areas in terms of flow depths.

The frequency characteristics of the pressure signals were examined by means of spectra. The results showed that the spectra of the drag fluctuations exhibit a different behaviour from those of the lift fluctuations. A $f^{-11/3}$ slope was observed for the spectra of the drag fluctuations over most of the frequency range, whereas the lift spectra suggest two scaling ranges, following a $f^{-11/3}$ slope at high frequencies ($f > 90$ Hz) and $f^{-5/3}$ behaviour at lower frequencies ($20$ Hz $< f < 90$ Hz). The results also show that the spectral magnitudes of both the drag and lift fluctuations increase with submergence and bed slope.

Until now, very few studies with detailed pressure measurements have been reported for open-channel turbulent flows. This limitation is due to the technical difficulties that are encountered for pressure measurement devices. The results from the present study, however, show that the small size, high sensitivity and accuracy of piezo-resistive pressure sensors provide useful measurements of pressure fluctuations on single sediment particles in open-channel turbulent flows. The array of sensors used in this study allowed the estimation of not only time-averaged statistics but also spatially averaged statistics. In turbulent flows, the particle lift and drag forces result from pressure differences across the particles. The four-point pressure technique employed in this study therefore provides a suitable way of predicting the behaviour of the lift and drag forces acting on sediment particles. The pressure fluctuation measurements have also provided additional insight into the interaction between turbulent flow and bed particles through the determination of pressure statistics, spatial and temporal characteristics and spectra. As direct measurement of near-bed pressure is more practicable than measurement of local bed shear stress, pressure measurements can be used to assist future investigations of particle transport and entrainment. The present findings can also be used to improve the prediction of sediment entrainment by analytical approaches as well.

## REFERENCES

ADRIAN, A. J. 2007 Hairpin vortex organisation in wall turbulence. *Phys. Fluids* **19** (4), 1–16.

ADRIAN, A. J. & MARUSIC, I. 2012 Coherent structures in flow over hydraulic engineering surfaces. *J. Hydraul Res.* **50** (5), 451–464.

BAJSIC, I., KUTIN, J. & ZAGAR, T. 2007 The response time of a pressure measurement system with a connecting tube. *Instrum. Sci. Technol.* **35**, 399–409.

BLAKE, W. K. 1970 Turbulent boundary-layer wall-pressure fluctuations on smooth and rough walls. *J. Fluid Mech.* **44** (4), 637–660.

BURTON, T. E. 1973 Wall pressure fluctuations at smooth and rough surfaces under turbulent boundary layers with favourable and adverse pressure gradients. *Report* Ad-772 548. Office of Naval Research.

CAMERON, S. M. 2006 Near boundary flow structure and particle entrainment. PhD dissertation, University of Auckland, New Zealand.

CAMERON, S. M. 2011 PIV algorithms for open-channel turbulence research: accuracy, resolution and limitations. *J. Hydro-Environ. Res.* **5** (4), 246–262.

CAMERON, S. M. & NIKORA, V. 2008 Eddy convection velocity for smooth- and rough-bed open-channel flows: particle image velocimetry study. In *River Flow 2008, Proceedings of the International Conference on Fluvial Hydraulics, Cesme-izmir-Turkey*, pp. 143–150. A. A. Balkema.

CAMERON, S. M., NIKORA, V. I., ALBAYRAK, I., MILER, O., STEWART, M. & SINISCALCHI, F. 2013 Interactions between aquatic plants and turbulent flow: a field study using a stereoscopic PIV system. *J. Fluid Mech.* **732**, 345–372.

CANTWELL, B. J. 1981 Organised motion in turbulent flow. *Rev. Fluid Mech.* **13**, 457–515.

CELIK, A. O., DIPLAS, P. & DANCEY, C. 2014 Instantaneous pressure measurements on a spherical grain under threshold flow conditions. *J. Fluid Mech.* **741**, 60–97.

CHAN-BRAUN, C. 2012 Turbulent open channel flow, sediment erosion and sediment transport. PhD dissertation, University of Karlsruhe, Germany.

CHAN-BRAUN, C., VILLALBA, M. G. & UHLMANN, M. 2011 Force and torque acting on particles in a transitionally rough open channel flow. *J. Fluid Mech.* **684**, 441–474.

CHAN-BRAUN, C., VILLALBA, M. G. & UHLMANN, M. 2013 Spatial and temporal scales of force and torque acting on wall-mounted spherical particles in open channel flow. *Phys. Fluids* **25**, 075103.

CHEPIL, W. S. 1958 The use of evenly spaced hemispheres to evaluate aerodynamic forces on a soil surface. *EOS Trans. AGU* **39**, 397–404.

CHEPIL, W. S. 1961 The use of spheres to measure lift and drag on wind-eroded soil grains. *Soil Sci. Soc. Am. J.* **25**, 343–345.

COLEMAN, N. L. 1967 A theoretical and experimental study of drag and lift forces acting on a sphere resting on a hypothetical stream bed. In *Proceedings of 12th IAHR Congress*, vol. 3, pp. 185–192. Fort Collins.

COLEMAN, N. L. & ELLIS, W. M. 1976 Model study of the drag coefficient of a streambed particle. In *Proceedings of 3rd Federal Interagency Sedimentation Conference, Denver, USA*. Water Resources Council, National Technical Information Service, Springfield, VA, USA, 4/1–4/11.

DETERT, M. 2008 Hydrodynamic processes at the water–sediment interface of streambeds. PhD thesis, University of Karlsruhe, Germany.

DETERT, M., JIRKA, G. H., KLAR, M., JEHLE, M., JAHNE, B., KOHLER, H.-J. & WENKA, T. 2004 Pressure fluctuations within subsurface gravel bed caused by turbulent open-channel flow. In *River Flow 2004, Proceedings of the International Conference on Fluvial Hydraulics, Napoli* (ed. M. Greco, A. Carravetta & R. Della Morte). A. A. Balkema.

DETERT, M., WEITBRECHT, V. & JIRKA, G. H. 2010a Laboratory measurements on turbulent pressure fluctuations in and above gravel beds. *J. Hydraul. Engng ASCE* **136** (10), 779–789.

DETERT, M., NIKORA, V. & JIRKA, G. H. 2010b Synoptic velocity and pressure fields at the water–sediment interface of streambeds. *J. Fluid Mech.* **660**, 55–86.

DIPLAS, P., DANCEY, C. L., CELIK, A. O., VALYRAKIS, M., GREER, K. & AKAR, T. 2008 The role of impulse on the initiation of particle movement under turbulent flow conditions. *Science* **322**, 717–720.

DWIVEDI, A. 2010 Mechanics of sediment entrainment. PhD thesis, University of Auckland, New Zealand.

DWIVEDI, A., MELVILLE, B. & SHAMSELDIN, A. Y. 2010 Hydrodynamic forces generated on a spherical sediment particle during entrainment. *J. Hydraul. Engng ASCE* **136**, 756–769.

ECKLEMANN, H. 1988 A review of knowledge on pressure fluctuations. In *Proceedings of Zoran Zaric Memorial International Seminar on Near-Wall Turbulence, Dubrovnik, Yugoslavia*, vol. 28, pp. 328–347.

EINSTEIN, H. A. & EL-SAMNI, E. A. 1949 Hydrodynamic forces on a rough wall. *Rev. Mod. Phys.* **21** (3), 520–523.

FARABEE, T. M. & CASARELLA, M. J. 1991 Spectral features of wall pressure fluctuations beneath turbulent boundary layers. *Phys. Fluids* **3**, 2410–2420.

GARCIA, C. M., JACKSON, P. R. & GARCIA, M. H. 2006 Confidence intervals in the determination of turbulence parameters. *Exp. Fluids* **40**, 514–522.

GARCIA, M., NINO, Y. & LOPEZ, F. 1995 Characterisation of near-bed coherent structures in turbulent open channel flow using synchronised high-speed video and hot-film measurements. *Exp. Fluids* **19**, 16–28.

GARCIA, M., NINO, Y. & LOPEZ, F. 1996 Laboratory observations of particle entrainment into suspension by turbulent bursting. In *Coherent Flow Structures in Open Channels* (ed. P. J. Ashworth, S. J. Bennet, J. I. Best & S. J. McLelland), pp. 63–84. Wiley.

GEORGE, W. K., BEUTHER, P. D. & ARNDT, R. E. A. 1984 Pressure spectra in turbulent free shear flows. *J. Fluid Mech.* **148**, 148–191.

GRASS, A. J. 1971 Structural features of turbulent flow over smooth and rough boundaries. *J. Fluid Mech.* **50**, 230–255.

HINZE, J. O. 1975 *Turbulence*. McGraw-Hill.

HOFLAND, B. 2005 Rock and roll, turbulence-induced damage of granular bed predictions. PhD thesis, Delft University of Technology, The Netherlands.

HOFLAND, B., BATTJES, J. & BOOIJ, R. 2005 Measurement of fluctuating pressures on coarse bed material. *J. Hydraul. Engng ASCE* **131** (9), 770–781.

HUSSAIN, A. K. M. F. 1986 Coherent structures and turbulence. *J. Fluid Mech.* **173**, 303–356.

IRWIN, H. P. A. H., COOPER, K. R. & GIRARD, R. 1979 Correction of distortion effects caused by tubing systems in measurements of fluctuating pressures. *J. Wind Engng Ind. Aerodyn.* **5**, 93–107.

KATUL, G. G. & PARLANGE, M. B. 1995 Analysis of land surface heat fluxes using the orthonormal wavelet approach. *Water Resour. Res.* **31**, 2743–2749.

KIM, J. 1989 On the structure of pressure fluctuations in simulated turbulent channel flow. *J. Fluid Mech.* **205**, 421–451.

KLINE, S. J. 1978 The role of visualisation in the study of the structure of the turbulent boundary layer. In *Lehigh Workshop on Coherent Structure of Turbulent Boundary Layers* (ed. C. R. Smith & D. E. Abbott), p. 126. Lehigh University.

KRAICHNAN, R. H. 1956 Pressure fluctuations in turbulent flow over a flat plate. *J. Acoust. Soc. Am.* **28**, 378–390.

LAMB, M. P., DIETRICH, W. E. & VENDITTI, J. G. 2008 Is the critical shields stress for incipient sediment motion dependent on channel-bed slope? *J. Geophys. Res.* **113**, F02008.

LEE, I. & SUNG, H. J. 2002 Multiple-arrayed pressure measurement for investigation of the unsteady flow structure of a reattaching shear layer. *J. Fluid Mech.* **463**, 377–402.

MANES, C., POKRAJAC, D. & MCEWAN, I. 2007 Double-averaged open-channel flows with small relative submergence. *J. Hydraul. Engng ASCE* **133** (8), 896–904.

MATTIOLI, M., ALSINA, J. M., MANCINELLI, A., MIOZZI, M. & BROCCHINI, M. 2012 Experimental investigation of the nearbed dynamics around a submarine pipeline laying on different types of seabed: the interaction between turbulent structures and particles. *Adv. Water Resour.* **48**, 31–46.

MOFFAT, R. J. 1988 Describing the uncertainties in experimental results. *Exp. Therm. Fluid Sci.* **1**, 3–17.

NELSON, J., SHREVE, R. L., MCLEAN, S. R. & DRAKE, T. G. 1995 Role of near-bed turbulence structure in bed load transport and bed-form mechanics. *Water Resour. Res.* **31** (8), 2071–2086.

NEZU, I. 2005 Open-channel flow turbulence and its research prospect in the 21st century. *J. Hydraul. Engng ASCE* **131** (4), 229–246.

NEZU, I. & NAKAGAWA, H. 1993 *Turbulence in Open-Channel Flows*. Balkema.

NIKORA, V. & GORING, D. 2000 Eddy convection velocity and Taylor's hypothesis of 'frozen' turbulence in a rough-bed open-channel flow. *J. Hydrosci. Hydraul. Engng* **18** (2), 75–91.

NIKORA, V., MCEWAN, I., MCLEAN, S., COLEMAN, S., POKRAJAC, D. & WALTERS, R. 2007a Double-averaging concept for rough-bed open-channel and overland flows: theoretical background. *J. Hydraul. Engng ASCE* **133** (8), 873–883.

NIKORA, V., MCLEAN, S., COLEMAN, S., POKRAJAC, D., MCEWAN, I., CAMPBELL, L., ABERLE, J., CLUNIE, D. & KOLL, K. 2007b Double-averaging concept for rough-bed open-channel and overland flows: applications. *J. Hydraul. Engng ASCE* **133** (8), 884–895.

NINO, Y. & GARCIA, M. H. 1996 Experiments on particle–turbulence interactions in the near-wall region of an open-channel flow: implications for sediment transport. *J. Fluid Mech.* **326**, 285–319.

POKRAJAC, D., FINNIGAN, J. J., MANES, C., MCEWAN, I. & NIKORA, V. 2006 On the definition of the shear velocity in rough bed open channel flows. In *River Flow 2006, Proceedings of the International Conference on Fluvial Hydraulics, Lisbon, Portugal*, pp. 88–96. Taylor & Francis.

PRASAD, A. K. 2000 Stereoscopic particle image velocimetry. *Exp. Fluids* **29**, 103–116.

QUADRIO, M. & LUCHINI, P. 2003 Integral space–time scales in turbulent wall flows. *Phys. Fluids* **15** (8), 2219–2227.

RASHIDI, M., HETSRONI, G. & BANERJEE, S. 1990 Particle–turbulence interaction in a boundary layer. *Intl J. Multiphase Flow* **16**, 935–949.

RAUDKIVI, A. J. 1990 *Loose Boundary Hydraulics*, 3rd edn. Pergamon.

ROBINSON, S. K. 1991 Coherent motions in turbulent boundary layers. *Annu. Rev. Fluid Mech.* **13**, 601–639.

SCHEWE, G. 1983 On the force fluctuations acting on a circular cylinder in crossflow from subcritical to transcritical Reynolds numbers. *J. Fluid Mech.* **134**, 311–328.

SCHMEECKLE, M. W., NELSON, J. M. & SHREVE, R. L. 2007 Forces on stationary particles in near-bed turbulent flows. *J. Geophys. Res.* **112**, F02003.

SHIELDS, A. 1936 Anwendung der Ahnlichkeitsmechanik und der Turbulentzforschung auf die Geshiebebewegung, Mitt. Preuss. Versuchsanst. Wasserbau Schiffbau, vol. 26, 26 pp. (English translation by W. P. Ott & J. C. van Uchelen, 1936. *Rep. 167*, 36 pp., Calif. Inst. of Technol., Pasadena).

SINGH, K. M., SANDHAM, N. D. & WILLIAMS, J. J. R. 2007 Numerical simulation of flow over a rough bed. *J. Hydraul. Engng ASCE* **133**, 386–398.

SMART, G. M. 2005 A novel gravel entrainment investigation. In *Proceedings of the 4th IAHR Symposium on River, Coastal and Estuarine Morphodynamics, Urbana, Illinois, USA*. Taylor & Francis.

SMART, G. M. 2008 Pressure fluctuations and entrainment on a gravel bed. In *River Flow 2008, International Conference on Fluvial Hydraulics, Cesme-izmir-Turkey* (ed. M. S. Altinakar, M. A. Kokpinar, I. Aydin, S. Cokgor & S. Kirkgoz). A. A. Balkema.

SMART, G. M. & HABERSACK, H. M. 2007 Pressure fluctuations and gravel entrainment in rivers. *J. Hydraul Res.* **45** (5), 661–673.

STEWART, M. T. 2014 Turbulence structure of rough-bed open-channel flow. PhD dissertation, University of Aberdeen, UK.

SUMER, B. M. & DEIGAARD, R. 1981 Particle motions near the bottom in turbulent flow in an open channel. *J. Fluid Mech.* **109**, 311–338.

TOWNSEND, A. A. 1976 *The Structure of Turbulent Shear Flow*, 2nd edn. Cambridge University Press.

TRITTON, D. J. 1988 *Physical Fluid Dynamics*, 2nd edn. Oxford University Press.

TSUJI, Y., FRANSSON, J. H. M., ALFREDSSON, P. H. & JOHANSSON, A. V. 2007 Pressure statistics and their scaling in high-Reynolds-number turbulent boundary layers. *J. Fluid Mech.* **585**, 1–40.

VAN HOUT, R. 2013 Spatially and temporally resolved measurements of bead resuspension and saltation in a turbulent water channel flow. *J. Fluid Mech.* **715**, 389–423.

WELCH, P. D. 1967 The use of fast Fourier transform for the estimation of power spectra: a method based on time averaging over short, modified periodograms. *IEEE Trans. Audio Electroacoust.* **15**, 70–73.

WILLERT, C. 1997 Stereoscopic digital particle image velocimetry for application in wind tunnel flows. *Meas. Sci. Technol.* **8**, 1465–1479.

WILLMARTH, W. W. 1975 Structure of turbulence in boundary layers. *Adv. Appl. Mech.* **15**, 159–254.

WILLMARTH, W. W. & ROOS, F. W. 1965 Resolution and structure of the wall pressure field beneath a turbulent boundary layer. *J. Fluid Mech.* **22**, 81–94.

WILLMARTH, W. W. & WOOLDRIDGE, C. E. 1962 Measurements of the fluctuating pressure at the wall beneath a thick turbulent boundary layer. *J. Fluid Mech.* **14** (2), 187–210.

YOSHIDA, A., TAMURA, Y. & KURITA, T. 2001 Effects of bends in a tubing system for pressure measurement. *J. Wind Engng Ind. Aerodyn.* **89** (20), 1701–1716.

YUNG, B. P. K., MERRY, H. & BOTT, T. R. 1989 The role of turbulent bursts in particle re-entrainment in aqueous systems. *Chem. Engng Sci.* **44**, 873–882.